On the Role of VP3-PI3P Interaction in Birnavirus Endosomal Membrane Targeting

Flavia A. Zanetti[a,#], Ignacio Fernández[b,#]; Eduard Baquero[b]; Pablo Guardado-Calvo[b]; Andres Ferrino-Iriarte[b]; Sarah Dubois[c]; Etienne Morel[c]; Victoria Alfonso[d]; Milton O. Aguilera[e]; María E. Celayes[e]; Luis M. Polo[e]; Laila Suhaiman[f,†]; Vanesa V. Galassi[f,g]; María V. Chiarpotti[f,g,††]; Carolina Allende[h]; Javier M. Rodríguez[h]; José R. Castón[h]; Diego Lijavetzky[i]; Oscar Taboga[d]; María I. Colombo[e]; Mario G. Del Pópolo[f,g]; Félix A. Rey[b]; Laura R. Delgui[e,g,*]

[a] Instituto de Ciencia y Tecnología "Dr. Cesar Milstein", Consejo Nacional de Investigaciones Científicas y Técnicas (CONICET), Saladillo 2468 C1440FFX, Ciudad Autónoma de Buenos Aires, Argentina.

[b] Institut Pasteur, Université Paris Cité, Structural Virology Unit, 25-28 Rue du Dr. Roux, 75015 Paris, France.

[c] Université Paris Cité, INSERM UMR-S1151, CNRS UMR-S8253, Institut Necker Enfants Malades, Rue de Vaugirard 156, 75015 Paris, France.

[d] Instituto de Agrobiotecnología y Biología Molecular (IABIMO), Instituto Nacional de Tecnología Agropecuaria (INTA), Consejo Nacional de Investigaciones Científicas y Técnicas (CONICET), De los Reseros y N. Repetto s/n, Hurlingham B1686IGC, Buenos Aires, Argentina.

[e] Instituto de Histología y Embriología de Mendoza, Universidad Nacional de Cuyo (UNCuyo), Consejo Nacional de Investigaciones Científicas y Técnicas (CONICET), Centro Universitario M5502JMA, 5500 Mendoza, Argentina.

[f] Instituto Interdisciplinario de Ciencias Básicas (ICB), Consejo Nacional de Investigaciones Científicas y Técnicas (CONICET), Padre Contreras 1300, 5500 Mendoza, Argentina.

[g] Facultad de Ciencias Exactas y Naturales, Universidad Nacional de Cuyo (UNCuyo), Padre Contreras 1300, 5500 Mendoza, Argentina.

[h] Department of Structure of Macromolecules, Centro Nacional de Biotecnología (CNB-CSIC), C. Darwin, 3, 28049 Madrid, Spain.

[i] Instituto de Biología Agrícola de Mendoza, Universidad Nacional de Cuyo (UNCuyo), Consejo Nacional de Investigaciones Científicas y Técnicas (CONICET), Almirante Brown 500, M5528AHB. Chacras de Coria, Mendoza, Argentina.

[#]F.A.Z. and I.F. contributed equally to this work.

†Current affiliation: Instituto de Medicina y Biología Experimental de Cuyo (IMBECU) - Consejo Nacional de Investigaciones Científicas y Técnicas (CONICET), Facultad de Ciencias Médicas, Universidad Nacional de Cuyo (UNCuyo), Mendoza, Argentina.

††Current affiliation: AI Proteins, 20 Overland St., Boston MA 02215, USA.

*Laura R. Delgui

Email: ldelgui@mendoza-conicet.gob.ar; ldelgui@fcm.uncu.edu.ar

Author Contributions: I.F., E.B., F.A.R., M.G.D.P. and L.R.D. designed research; F.A.Z., P.G.C., A.F.I., S.D., E.M., V.A., M.O.A., M.E.C., L.M.P., L.S., V.V.G., M.V.C., C.A., J.M.R., and L.R.D. performed research; I.F., E.B., M.O.A., D.L., M.G.D.P., F.A.R., and L.R.D. analyzed data; J.R.C., O.T., M.I.C. and F.A.R. contributed new reagents/analytic tools; and L.R.D. and M.G.D.P. wrote the paper.

Competing Interest Statement: The authors declare no competing interest.

Keywords: Birnavirus - Endosomes - Membrane - Phosphatidylinositol-3-phosphate - Replication - Viral evolution.

Abstract

Birnaviruses are a group of double-stranded RNA (dsRNA) viruses infecting birds, fish and insects. Early endosomes (EE) constitute the platform for viral replication. Here, we study the mechanism of birnaviral targeting of EE membranes. Using the Infectious Bursal Disease Virus (IBDV) as a model, we validate that the viral protein 3 (VP3) binds to phosphatidylinositol-3-phosphate (PI3P) present in EE membranes. We identify the domain of VP3 involved in PI3P-binding, named P2 and localized in the core of VP3, and establish the critical role of the arginine at position 200 (R_{200}), conserved among all known birnaviruses. Mutating R_{200} abolishes viral replication. Moreover, we propose a two-stage modular mechanism for VP3 association with EE. Firstly, the carboxy-terminal region of VP3 adsorbs on the membrane, and then the VP3 core reinforces the membrane engagement by specifically binding PI3P through its P2 domain, additionally promoting PI3P accumulation.

Significance Statement

Birnaviruses are a family of viruses unique among the group of dsRNA viruses. Here, we show that VP3 seizes the endosomes by anchoring to the PI3P lipids in the luminal side of the EE membrane, in order to organize the viral replication factory. We propose a two-stage modular mechanism for VP3 association with PI3P-enriched EE. The significance of this work resides in the biochemical and biophysical insights on the mechanism of association of VP3 with EE and its role in the viral life cycle, which represents a substantial contribution toward understanding the replication strategy of these "*non-canonical*" viruses.

Introduction

Birnaviruses belong to the *Birnaviridae* family composed of nonenveloped icosahedral dsRNA viruses that infect a wide range of vertebrate and invertebrate hosts. The prototypical and best-characterized family member, the Infectious Bursal Disease Virus (IBDV), is the causative agent of Gumboro disease, a highly contagious immunosuppressive disease that affects young chickens (*Gallus gallus*) causing significant damage to the poultry industry (Delmas et al., 2019).

Birnaviruses are unconventional dsRNA viruses, as the virions lack a "*core",* i.e., an inner protein layer containing the genome, which instead forms a filamentous ribonucleoprotein complex (RNP) with the multifunctional protein VP3, the RdRp VP1, and the dsRNA genome segments (Luque et al., 2009b). IBDV contains a single ~70-nm diameter T = 13*l* icosahedral capsid surrounding a polyploid bipartite dsRNA genome (segments A and B, 3.2 and 2.8 kbp, respectively) (Luque et al., 2009a). The X-ray crystal structure of the capsid revealed that VP2 is the only component. VP2 has two main domains, a "shell" domain homologous to the coat proteins of +sRNA such as the T = 3 nodaviruses, and a "tower" domain, like those present in the T = 13 middle-layer protein of dsRNA viruses of the order *Reovirales* (Coulibaly et al., 2005). VP3 is a 257-residues long polypeptide that plays multiple roles during the viral life cycle. In the mature virion, VP3 is a component of the RNPs, where it is associated with the dsRNA (Luque et al., 2009b). During viral assembly, VP3 acts as a scaffold protein via electrostatic interactions between basic residues of pVP2 (the precursor form of VP2), and acidic residues at the VP3 carboxy-terminal (Ct) region (Saugar et al., 2010). Additionally, VP3 interacts with VP1 (Lombardo et al., 1999). VP3's multifunctional properties might be mediated by its capacity to form oligomers (Casañas et al., 2008), or by its intrinsically disordered regions. The X-ray crystal structure of the central region of the IBDV VP3 (residues 82 to 222) showed that it consists entirely of α-helices connected by loops which

can be divided into two structural domains linked by a flexible hinge. The 36 Ct residues of the protein, a highly hydrophilic region rich in charged amino acids and proline residues, were predicted to be disordered, so it was excluded from the crystallized construct. The 81 amino-terminal (Nt) region of VP3 was cleaved during the crystallization process and was absent in the crystal (Casañas et al., 2008). The X-ray crystal structure indicated the presence of two positively charged domains, termed Patch 1 (P1) and Patch 2 (P2) (Valli et al., 2012). Both patches are composed of four discontinuous, positively charged residues forming two exposed patches on the surface of the protein. P1 was demonstrated to be involved in the dsRNA binding-activity of VP3 (Valli et al., 2012).

Previous studies on the subcellular localization of the IBDV replication complex (RC) have shown that IBDV replication components are localized to EE (Delgui et al., 2013). Further analysis revealed that VP3 associates with the cytosolic leaflet of EE membranes via P2, with a critical functional role in the virus life cycle (Gimenez et al., 2018). Additionally, the presence of PI3P in EE membranes was demonstrated to be a key host factor for VP3 association and the consequent establishment of IBDV RCs on EE membranes (Gimenez et al., 2020).

Here we study the mechanism mediating the birnaviral targeting of EE membranes, focusing on the VP3-PI3P interaction. Using biophysical approaches in cell-free *in vitro* systems, we demonstrate that PI3P constitutes the cellular partner for VP3 association to EE membranes. By introducing charge-reversal point mutations on VP3 P2, we establish the contribution of each of the four positively charged residues composing P2, with a key role of the arginine at position 200 (R_{200}), a residue conserved across all known birnaviruses. Using a reverse genetic system for IBDV, we show that mutating R_{200} abolishes viral replication. Finally, by using molecular simulations, we discuss a potential two-stage modular mechanism for VP3 association with EE. We show that, in the first step, the Ct flexible tail of VP3 adsorbs to the membrane by electrostatic interactions due to its positive charge. Then, in the second stage,

the VP3 core reinforces the membrane engagement by recruiting PI3P molecules scattered in the EE membrane to the P2 region, promoting a stable VP3-PI3P interaction.

Results

Biophysical characterization of VP3 binding to PI3P. We set up a liposome co-flotation assay to assess the binding of VP3 to PI3P in membranes. We expressed and purified His-tagged VP3 full-length (His-VP3 FL) and confirmed its identity by Western blot using specific anti-VP3 and anti-His antibodies. Since we observed four different bands for the purified protein, we confirmed their VP3-identity by mass spectrometry (*SI Appendix*, Fig. S1). We prepared two populations of liposomes: "liposomes PI3P(-)" and "liposomes PI3P(+)". We confirmed that these preparations were suitable for evaluating the interaction with PI3P by monitoring co-flotation of a recombinant His-2xFYVE domain (Fab1p, YOTB, Vac1p, and EEA1), followed by immunoblot detection of the His-tag. FYVE domains are highly homologous cysteine-rich domains of 70-80 amino acids present in around 30 human proteins that are known to participate in vesicular sorting or endocytosis through direct binding to PI3P from EE (Burd and Emr, 1998; Gaullier et al., 1998; Simonsen et al., 1998; Stenmark et al., 1996) (**Fig. 1A**). We observed specific binding of His-VP3 FL to liposomes PI3P(+), evidenced by a significant difference in the ability to bind to both liposome populations (**Fig. 1B**). To test His-VP3 FL PI3P-binding specificity, we performed a co-flotation assay using liposomes where PI3P was replaced by 1,2-dioleoyl-sn-glycero-3-phosphate ("liposomes PA") or [1,2-dioleoyl-sn-glycero-3-phospho-(1'-myo-inositol)] ("liposomes PI") at the same molar ratio. PA contains a POH_4^- group also present in the polar head of PI3P but lacks the inositol ring, while PI has the inositol ring but is not phosphorylated. We observed that His-VP3 FL bound to liposomes PI3P(+), but not to liposomes PA or PI, reinforcing the notion that a phosphoinositide

is required since neither a single negative charge nor an inositol ring are sufficient to promote VP3 binding to liposomes (*SI Appendix*, Fig. S2).

Two additional biophysical approaches were implemented. First, we prepared liposomes PI3P(-) and PI3P(+), and incubated them with His-2xFYVE or His-VP3 FL that had been pre-bound to Ni-NTA [nickel (II) nitrilotriacetic acid] gold particles. Subsequently we inspected the preparations by cryo-electron microscopy (cryo-EM). Gold particles were not observed on liposomes PI3P(-) incubated with either protein (**Fig, 1C, left panel**). We observed gold particles decorating liposomes PI3P(+) in the presence of both, His-2xFYVE and His-VP3 FL (**Fig. 1C, right panel**). Second, we performed bio-layer interferometry (BLI) experiments using purified His-VP3 FL, and liposomes PI3P(-) and PI3P(+) (Shah et al., 2014). In the BLI experiments, the protein is immobilized on the tip of Ni-NTA sensors while the liposomes remain in solution, allowing to monitor the molecular interactions in real-time (Kairys et al., 2019). Purified His-Streptavidin and His-2xFYVE were used as negative and positive controls, respectively. A specific liposome PI3P(+) dose-dependent binding of His-2xFYVE and His-VP3 FL was observed (**Fig. 1D**).

Previous studies indicated that the P2 is responsible for PI3P binding on EE membranes (Gimenez et al., 2020, 2018). Yet the Ct region of VP3 is also highly enriched in positively charged residues. We generated a computational model of FL VP3 using AlphaFold2 (Jumper et al., 2021), which predicted a disordered Ct region (pLDTT of 42.6) (**Fig. 1E**). Thus, we hypothesized that both conditions, the positive electrostatic surface charge and the disordered character of the VP3 Ct, might be contributing to the binding to the surface of EE. To test this hypothesis, we made a VP3 construct bearing a Ct truncation (His-VP3 ΔCt) and used it in co-flotation assays and BLI experiments. We did not detect interaction of this mutant with PI3P(-) nor PI3P(+) liposomes (**Fig. 1F, G**). Taken together, our results validate the

role of PI3P in the interaction with VP3 and underscore the significance of the Ct domain in mediating this interaction.

Role of VP3 P2 in the association of VP3 with the EE membrane. Inspection of the VP3 crystal structure showed that P2 residues (K_{157}, R_{159}, H_{198} and R_{200}) form a positive-charged groove on the protein surface (**Fig. 2A-B**). We prepared VP3 point mutants with reversed charge in a pcDNA vector backbone, giving rise to pcDNA VP3 $K_{157}D$, $R_{159}D$, $H_{198}D$ and $R_{200}D$. The calculated electrostatic potential of P2 for each of these mutants is shown in **Fig. 2C**. Firstly, we used QM7 cells transiently overexpressing VP3 P2 Wild Type (WT), P2 (all reversed) or the four single mutation of P2 to quantitatively assess their cellular distribution. We observed a punctuated distribution of VP3 P2 WT, $K_{157}D$, $R_{159}D$ and $H_{198}D$. In contrast, the specific indirect immunofluorescence (IIF) signal of VP3 P2 all reversed and $R_{200}D$ showed a diffuse cytosolic distribution (**Fig. 2D, panels framed in red**). Secondly, we assessed the distribution of the VP3 constructs in QM7 cells transiently overexpressing EGFP-Rab5. Rab5 regulates the homotypic tethering and fusion of EEs, and it is considered a genuine marker of EEs (Gorvel et al., 1991). As observed in **Fig. 2E**, and the quantitative colocalization analysis (*SI Appendix*, Fig. S3), VP3 P2 WT, $K_{157}D$, $R_{159}D$ and $H_{198}D$ showed a marked colocalization with EGFP-Rab5. In contrast, the VP3 P2 all reversed and $R_{200}D$-derived IIF signal indicated a cytosolic distribution (**Fig. 2E, panels framed in red)**. It is important to mention that the differences in co-localization shown in Fig. S3 are small and not significant, but still show a trend that correlates with observations depicted in **Fig. 2D**. Taken together, these results suggest that R_{200} in the P2 patch bears a critical role in the association of VP3 with EE membranes.

VP3 P2 mediates VP3-PI3P association to EE membranes. To further assess the contribution of P2 residues to PI3P binding, and to strengthen the observations made on cells transiently overexpressing EGFP-Rab5, we set up two additional cell biology assays. One consists of co-transfecting cells with EGFP-2xFYVE and VP3 constructs, and detecting them by confocal laser scanning microscopy (CLSM). The second one consists of assessing the ability of purified GST-2xFYVE, which recognizes endogenous PI3P, to co-localize with VP3. We employed QM7 cells transiently co-overexpressing EGFP-2xFYVE and VP3 P2 WT, P2 all reversed, or the four point mutants to evaluate their colocalization. As shown in **Fig. 3A**, we observed a punctuated distribution with a marked co-localization with EGFP-2xFYVE for VP3 P2 WT while for VP3 P2 all reversed the IIF signal indicated a cytosolic distribution of the protein with the loss of colocalization with EGFP-2xFYVE (**Fig. 3A, red framed panels on the upper two rows**). Regarding the point mutants, we observed a loss of punctuated distribution and EGFP-2xFYVE co-localization for VP3 FL $R_{200}D$ (**Fig. 3A, red framed panels on the bottom row**). Then, we used the GST-2xFYVE purified domain to recognize endogenous PI3P in fixed cells (Nascimbeni et al., 2017). GST-2xFYVE was used as the "primary antibody", which was labelled with a fluorescent anti-GST antibody. As an additional control in these experiments, we immunostained the EE with antibodies anti-EEA1. As shown in **Fig. 3B**, VP3 P2 WT demonstrated a conspicuous PI3P-bearing EEA1 positive endosomes location. In addition, we observed a similar distribution for VP3 K_{157D}, $R_{159}D$, and $H_{198}D$ and a drastic change in VP3 FL $R_{200}D$ mutant, which appeared utterly cytosolic, losing its capacity to bind to PI3P-bearing EE membranes (**Fig. 3B, red framed panel on the lowest row**). These results further support the role of R_{200} in this interaction.

VP3 R_{200} is crucial for binding to PI3P. To validate this, we devised a liposome co-flotation assay using a recombinant His-VP3 FL $R_{200}D$ mutant. When assayed in parallel with His-2xFYVE, we

observed that His-VP3 FL $R_{200}D$ lost binding to PI3P(+) liposomes (**Fig. 4A**). To confirm that the lack of binding was not due to misfolding of the mutant, we compared the circular dichroism spectra of His-VP3 FL and His-VP3 FL $R_{200}D$ proteins, without detecting significant differences (**Fig. 4B**). To assess its relevance in IBDV infectivity, we resorted to an IBDV reverse genetics system, based on a modification of the system described by Qi and coworkers (Qi et al., 2007). The full length sequences of the IBDV RNA segments A and B, flanked by a hammerhead ribozyme at the 5'-end and the hepatitis delta ribozyme at the 3'-end, were expressed under the control of an RNA polymerase II promoter within the plasmids pCAGEN.Hmz.SegA.Hdz (SegA) and pCAGEN.Hmz.SegB.Hdz (SegB). For this specific experiment we generated a third plasmid, pCAGEN.Hmz.SegA.$R_{200}D$.Hdz (SegA.$R_{200}D$), harboring a mutant version of segment A cDNA containing the $R_{200}D$ substitution. Then, QM7 cells were transfected with the plasmids SegA, SegB or Seg.$R_{200}D$ alone (as controls) or with a mixture of plasmids SegA+SegB (wild type situation) or SegA.$R_{200}D$+SegB (mutant situation). At 8 h post transfection (p.t.), when the new viruses have been able to assemble out of the two segments of RNA, the cells were recovered and re-plated onto fresh non-transfected cells to reveal the presence of infective viruses. At 72 h post-plating, the generation of foci forming units (FFUs) was revealed by Coomassie staining. As expected, single-transfections of SegA, SegB or Seg.$R_{200}D$ did not produce FFUs. As shown in **Fig. 4C**, the transfection of SegA+SegB produced detectable FFUs (the three circles in the upper panel) while no FFUs (the three circles in the lower panel) were detected after the transfection of SegA.$R_{200}D$+SegB (**Fig. 4C**). Given the relevance of VP3 R_{200}, we assessed its conservation among members of the *Birnaviridae* family. For this, a multiple sequence alignment of VP3 reference sequences was performed (*SI Appendix*, Fig. S4A). As shown, IBDV VP3 has 32-39% identity to the other selected homologues (*SI Appendix*, Fig. S4B). A closer look at the VP3 P2 revealed the complete conservation of R_{200} (**Fig. 4D**). Taken together, these findings show that VP3 R_{200} plays an important role mediating the VP3-PI3P

interaction, highlighting the active participation of EE membranes during the infectious cycle of birnaviruses.

Electrostatic forces mediate VP3 membrane binding. Computer simulations based on coarse-grain models were performed to assess the binding free-energy and adsorption mechanism of three protein variants: VP3 Ct, VP3 ΔNt, and VP3 FL. The VP3 Ct region, with a positive electrical charge of +5, was modeled as an intrinsically disordered region according to the AlphaFold2 prediction (**Fig. 1E**). VP3 ΔNt encompasses residues 82 to 257 and is electroneutral. This variant was chosen primarily because it retains the structural data from the crystallized protein. Similarly to His-VP3 FL, His-VP3 ΔNt retains the ability to bind to liposomes PI3P(+) (see *SI Appendix*, Fig. S5). Finally, VP3 FL is the full length monomeric VP3, using the AlphaFold2 predicted structure with an overall electrostatic charge of -3. We employed the Molecular Theory (MT) approach to obtain adsorption free-energy profiles, PMF(z), at different salt concentrations (Chiarpotti et al., 2021; Ramírez et al., 2019). The membrane was modeled as a rigid dielectric slab with 5% of its surface occupied by ternary ionizable groups. **Figure 5** (panels A-C) shows the PMF(z), where z represents the distance between the center of mass of the protein and the center of the membrane, at 50 and 150 mM NaCl. As observed in **Fig. 5A**, the positively charged VP3 Ct shows the highest affinity for the membrane due to the deprotonation of the acidic lipids at pH 8, resulting in a net negative charge on the membrane surface (*SI Appendix*, Fig. S6). However, the electroneutral construct VP3 ΔNt has a lower binding energy than VP3 Ct, and also VP3 FL shows some degree of membrane binding, despite both the protein and the membrane being negatively charged, as evidenced by the shallow minimum in the PMF.

The binding of the three protein constructs was strongly affected by electrostatics, as shown in **Fig. 5D**, where the adsorption energy is plotted as a function of the concentration of salt. The effect of salt

concentration is most significant for VP3 Ct, but it is also noticeable for VP3 ΔNt and VP3 FL. Also, the interfacial concentration of each construct was higher at lower ionic strengths, as depicted in *SI Appendix*, Fig. S7. The weak binding energy of VP3 FL to the anionic membrane under physiological conditions (~150 mM NaCl, pH 7) was consistent with the experimental observation that VP3 FL did not bind to liposomes PA and PI, which are anionic at the pH of the experiments. However, those same experiments showed that VP3 FL did bind to PI3P(+) liposomes (**Fig. 1B-C**), despite the MT calculations predicting weak binding. Taken together, our results suggest that specific VP3-PI3P interactions enhance the binding of VP3 to PI3P-containing EE membranes, while exhibiting weak and non-specific electrostatic attractions to an otherwise generic anionic membrane. *SI Appendix*, Fig. S8 illustrates the distribution of cationic residues of VP3 near the membrane, indicating that the Ct fragment drives the non-specific binding. To identify the electrical charge of different protein regions, *SI Appendix* Fig. S9 shows a map of the electrostatic potential around VP3 FL.

Molecular Dynamics (MD) simulations based on the MARTINI model were employed to further investigate the mechanism by which VP3 Ct and VP3 ΔNt approach the membrane surface. We chose VP3 ΔNt over VP3 FL because VP3 ΔNt has a closer resemblance to the well-established experimental crystal structure. Additionally, the adsorption free energy profiles predicted by MT for both VP3 ΔNt and VP3 FL are notably similar (compare panels B and C of Figure 5). Unlike the MT model, MARTINI considers both electrostatic and van der Waals forces (De Jong et al., 2013). To mimic the liposome PI3P(+) composition used in the co-flotation assays, the lipid bilayer was modeled with a molar ratio of 64:31:5 for the lipids DOPE, DOPC, and PI3P, respectively. DOPE and DOPC are electroneutral, PI3P is anionic. The MD simulations revealed that both VP3 Ct and VP3 ΔNt settled on the membrane surface after 120 ns, as shown in *SI Appendix*, Fig. S10. **Figure 6A-D** shows a temporal sequence of configurations during the adsorption of VP3 ΔNt. The protein approached the membrane via the Ct

fragment and remained adsorbed during the rest of the 500 ns trajectory. VP3 Ct exhibited the same behavior, as demonstrated in *SI Appendix*, Fig. S10 and Fig. S11. Notably, VP3 Ct and VP3 ΔNt did not detach from the surface during these MD simulations, suggesting that the adsorption energies calculated by MT were underestimated and represent a lower bound, as van der Waals interactions are absent in the MT model. Also, **Fig. 6E** highlights the location of the four positive residues that make up the P2 region, showing their proximity to the membrane surface.

Recruitment of PI3P modulates the membrane binding of VP3. We investigated the impact of VP3 Ct and VP3 ΔNt on the composition of the membrane near the binding point, and on the local curvature of PI3P(+) liposomes. We resorted to our MD simulations and evaluated the in-plane radial distribution function, g(r), between the center of mass of the proteins and the center of mass of PI3P molecules in the (cis) hemilayer, which is in direct contact with the protein. **Figure 6F** shows that VP3 Ct recruits PI3P within a ~2 nm radius, where its local concentration in the cis hemilayer is up to 6 times greater than the average PI3P concentration (*SI Appendix*, Fig. S12). Also, despite having no net electrical charge, VP3 ΔNt induces a similar concentration enhancement, with PI3P accumulation occurring around the Ct fragment, as evidenced in *SI Appendix*, Fig. S13. In both cases, the recruitment of PI3P in the cis hemilayer is accompanied by a local depletion of PI3P in the trans hemilayer, due to interhemilayer electrostatic repulsions. The effects on PI3P concentration, induced by VP3 ΔNt, result from a synergistic action between the positively charged Ct and the P2 region of the protein. Furthermore, when mutations are introduced to the P2 region - starting with $R_{200}D$ and eventually including the entire P2 domain - there is a gradual reduction in its contribution to the recruitment of PI3P (see *SI Appendix*, Fig. S14). Molecular Theory calculations on these mutants also reveal that the binding free energy of both VP3 ΔNt P2 Mut and VP3 ΔNt $R_{200}D$ is consistently lower than that of VP3 ΔNt across all salt concentrations

explored (see SI Appendix, Fig. S15). This indicates a weakening of the interaction with the negatively charged membrane, concomitant with the loss of positively charged amino acids.

Finally, to examine the potential impact of VP3 on the lipid bilayer, we incubated liposomes PI3P(-) and PI3P(+) with purified His-VP3 FL as described previously. The samples were cryo-fixed and cryo-EM was used to observe the resulting structures. As shown in **Fig. 6G**, His-VP3 FL distorts the membrane of liposomes containing PI3P, resulting in small pinches in the bilayer, detectable in 36% of the liposomes PI3P(+), while it is completely absent in PI3P(-) liposomes. Taken together, our findings suggest that the binding of VP3 to EE membranes has the potential to alter the local lipid composition by recruiting PI3P, which could then lead to the localized membrane pinches observed in **Figure 6G**.

Discussion

Several viruses hijack the PI3P metabolism machinery to complete their infectious cycle. However, only a few cases of viral proteins that bind PI3P have been described. Equine infectious anemia virus (EIAV) is a member of the lentivirus subgroup of retroviruses and replicates in macrophages. Retroviral assembly and release are directed by the structural precursor polyprotein Gag (Wills and Craven, 1991). EIAV Gag localizes to both the cell interior and to the plasma membrane due to its high-affinity interaction with PI3P (Fernandes et al., 2011; Puffer et al., 1998; Tanzi et al., 2003). Moreover, mutation of K_{49}, a residue in the PIs-binding pocket of Gag inhibited the release of viral-like particles from the plasma membrane (Fernandes et al., 2011). Another example are the poxviruses, a family of cytoplasmic DNA viruses that also rely on intracellular membranes to develop their envelope, whose morphogenesis requires enzymes from the cellular phosphoinositide metabolic pathway (Mcnulty et al., 2010). For vaccinia virus (VACV), the prototypic poxvirus, Kolli and coworkers showed that the VACV H7 protein binds to PI3P and PI4P

(Kolli et al., 2015). Similarly to our observations in IBDV VP3, the authors uncovered two regions of H7 essential for viral replication. One region is a positive surface patch centered on K_{108}, and the other region is the flexible Ct tail (Kolli et al., 2015).

Our biophysical and molecular simulation results suggest a specific but weak interaction of VP3 with PI3P bearing membranes. In co-floatation assays, we observed that His-VP3 FL reaches the top of the gradient, where liposomes PI3P(+) are located, with a high proportion of protein still found at the bottom of the gradient. This phenomenon was not observed with the His-2xFYVE protein. Additionally, the slopes of the BLI curves show that His-VP3 FL dissociate faster than His-2xFYVE from liposomes PI3P(+). Computer simulations have also revealed a weak attractive interaction between the negatively charged VP3 and membranes that contain PI3P. VP3 bears multiple essential roles during the viral life cycle. In this context, our hypothesis is that an early, specific, but weak interaction with PI3P is required for the formation of RCs associated with EE and represents an advantage for the virus that counts with VP3 to go forward into the replication cycle.

We identified the domain of VP3 involved in PI3P-binding, and established the critical role played by the arginine residue at position 200 of VP3 (R_{200}) . This arginine is conserved among all known birnaviruses. Mutating R_{200} abolishes viral replication. As previously mentioned, VP3 is a multifunctional viral protein. Therefore, it was initially possible that mutating R_{200} might affect other functions beyond PI3P binding and viral replication. However, R_{200} is not located in any of the protein regions associated with its other known functions. For instance, the VP3 dimerization domain, located in the second helical domain, involves 81 interprotomeric contacts across three helices, but R_{200} does not participate in these contacts (Casañas et al., 2008). Also, VP3 has an oligomerization domain mapped within the 42 C-terminal residues of the polypeptide, i.e., the segment of the protein composed by the residues at positions 216-257 (Maraver et al., 2003); VP3's ability to bind RNA is facilitated by a region

of positively-charged amino acids, identified as P1, which includes K_{99}, R_{102}, K_{105}, and K_{106} (Valli et al., 2012). Furthermore, our findings indicate that the $R_{200}D$ mutant retains a folding pattern similar to the wild-type protein. All these lead us to conclude that the loss of replication capacity of $R_{200}D$ viruses results from impaired, or even loss of, VP3-PI3P interaction.

It has recently been reported that the RCs of IBDV exhibit liquid-liquid phase separation (LLPS) (Reddy et al., 2022). In LLPS, one or more biomolecules form a network of mild homo- and heterotypic interactions, resulting in the formation of a distinct liquid phase within a liquid medium (Banani et al., 2017). In light of our results, it is conceivable to hypothesize that viral interaction with the EE membranes acts as a first step in the RCs biogenesis, leading to the growth of biomolecular condensates with LLPS characteristics around EE membranes, as recently proposed (Brodrick and Broadbent, 2023). In support of this model, both the RNA dependent RNA polymerase VP1 and the viral dsRNA associate to endosomes and to the LLPS condensates (Delgui et al., 2013; Reddy et al., 2022). Further experiments are needed in order to link the association of VP3 to EE membranes with biomolecular condensate formation.

Evolutionary links between +sRNA and dsRNA viruses

Birnaviruses integrate the double-strand RNA Baltimore group (Baltimore, 1971), and the newly created *Riboviria* taxon (a realm), that includes all RNA viruses encoding RdRps (Walker et al., 2021). However, the organization of the birnaviral RdRp (Gorbalenya et al., 2002) and the structure of its capsid (Coulibaly et al., 2005) had already indicated strong links between birnaviruses and +sRNA viruses, placing them in a special branch of the dsRNA viruses that appears to have evolved independently of the others. The membrane association of their replication complexes is a further specificity of birnaviruses that links them more to the +sRNA viruses than to the other dsRNA viruses. Indeed, within the megataxonomy

merging together Baltimores´ and Linnean classifications proposed by Koonin *et al*., the *Birnaviridae* family status is uncertain (Koonin et al., 2020).

Materials and Methods

Recombinant prokaryotic-expression plasmid. We used an *Escherichia coli*-based prokaryotic system to obtain the His-2xFYVE and GST-2xFYVE fusion proteins. For the first one, the plasmid encoding EGFP-2xFYVE, pEGFP-2xFYVE, generated by Gillooly and collaborators (Gillooly et al., 2000) was kindly provided by Harald A. Stenmark (Norwegian Radium Hospital, Oslo, Norway) to our group and used as a template. The 2xFYVE fingers consisted in duplicated domains of residues 147-223 of mouse hepatocyte growth factor-regulated tyrosine kinase substrate (Hrs) (Komada and Kitamura, 1995) separated by a QGQGS linker. The prokaryotic vector expressing 2xFYVE was obtained following standard PCR methods with the oligonucleotide pair 2xFYVE (*SI Appendix*, Table 1). The PCR fragment was inserted into the pET32a(+), which incorporates the thioredoxin A (TrxA) gene, a 6xHis tag and Thrombin site (Ts) within the amino-terminal domain of the 2xFYVE, and the correctness of the insertion was confirmed by sequencing. The complete fusion protein TrxA.His.Ts.2xFYVE (hereafter named His-2xFYVE) is 954 base pairs (bp)-long and contains 317 residues (~35 kDa). The plasmid encoding GST-2xFYVE was kindly gifted by Harald A. Stenmark (Norwegian Radium Hospital, Oslo, Norway) to the group of Etienne Morel.

Recombinant eukaryotic-expression plasmids. We used a *Baculovirus*-based eukaryotic system to obtain the His-VP3 FL, His-VP3 FL $R_{200}D$ and His-VP3 ΔCt fusion proteins. The construct of the recombinant baculovirus (rBV) His-VP3 FL was generated from IBDV VP3 FL protein [strain Soroa,

390 GenBank AF140705.1, residues 756-1012 (257 residues) from the polyprotein] cloned in pcDNA vector.
391 Thus, IBDV VP3 FL protein was subcloned from plasmid pcDNA VP3 FL into the pFast Bac HTb vector
392 (Gibco BRL), which incorporates a 6xHis tag at the N-terminal of the recombinant protein. Briefly, VP3
393 FL coding sequence was amplified by PCR with the oligonucleotide pairs VP3.Fw and VP3.Rv
394 incorporating *Bam*HI and *Eco*RI restriction sites, respectively (*SI Appendix*, Table 1). The resulting DNA
395 fragment containing the VP3 gene was digested with *Bam*HI and *Eco*RI and ligated to plasmid pFast Bac
396 HTb restricted with the same enzymes, generating the plasmid pFast Bac-his-VP3 FL. This plasmid
397 contained the VP3 gene fused to a histidine tag under the control of the polyhedrin promoter. The
398 complete fusion protein His-VP3 FL is 861 bp-long and contains 286 residues (~32 kDa). The generation
399 of rBV His-VP3 FL $R_{200}D$ was performed following the same procedure, but using the pcDNAVP3 FL
400 $R_{200}D$ as a template for subcloning. The complete fusion protein His-VP3 FL $R_{200}D$ is 861 bp-long and
401 contains 286 residues (~32 kDa). The generation of rBV His-VP3 Δ223-257 (His-VP3 ΔCt) was
402 performed as follows. A 663 nucleotide DNA fragment containing a truncated version of the VP3
403 sequence encoding a polypeptide lacking the 36 carboxi-terminal residues was amplified by PCR from
404 pcDNAVP3 FL with the oligonucleotide pairs VP3.Fw and VP3 Δ223-257.Rv incorporating *Bam*HI and
405 *Eco*RI restriction sites, respectively (*SI Appendix*, Table 1). The DNA fragment was digested with *Bam*HI
406 and *Eco*RI and was ligated to plasmid pFast Bac HTb restricted with the same enzymes, generating the
407 plasmid pFast Bac-his-VP3 Δ223-257, hereafter named His-VP3 ΔCt. All the resulting plasmids were
408 subjected to nucleotide sequencing to assess the correctness of the inserted VP3 sequence, and they were
409 then used to produce the corresponding rBVs by using the Bac-to-Bac system and by following the
410 manufacturer's instructions (Invitrogen). Briefly, the recombinant plasmids were transformed into
411 DH10Bac competent cells to obtain recombinant bacmids. The white colonies on culture plates were
412 picked, confirmed by PCR and used for Sf9 cell transfection by using Cellfectin II Reagent (Gibco). The

transfected cells were cultured at 28°C for 5 days to produce rBVs. Then, the cells were subjected to Western blot analysis for recombinant proteins expression confirmation and the supernatant (P1) was used to amplify the rBVs to a higher-titre P2 and scaled up to obtain a higher volume of P3 to be titrated (Plate-Forme Technologique Production et Purification de Protéines Recombinantes, Institut Pasteur) and used for protein production.

Protein expression and purification. His-VP3 polypeptides were produced in the Bac-to-Bac™ Baculovirus Expression System. Briefly, Sf9 cells (Gibco, ThermoFisher Scientific) were infected with recombinant Baculoviruses (rBVs) at a multiplicity of infection (MOI) of 5 PFU/cell. Cells were harvested at 96 h post-infection, washed once with chilled phosphate-buffered saline (PBS), resuspended in lysis buffer [50 mM Tris-HCl (pH 8.0), 500 mM NaCl, 0.1% nonidet P-40) supplemented with protease inhibitors (Complete Mini, Roche), and maintained on ice for 30 min. Thereafter, extracts were sonicated and centrifuged at 13.000 g for 15 min at 4ºC. Supernatants were collected and subjected to immobilized metal-affinity chromatography (IMAC) purification by using a Ni^{2+} affinity column (HiTrap Fast Flow Crude, GE Healthcare). Resin-bound proteins were eluted with elution buffer [50 mM Tris-HCl (pH 8.0), 500 mM NaCl, 500 mM imidazole]. His-tagged VP3 FL, VP3 ΔCt or VP3 FL $R_{200}D$ -containing fractions were pooled and subjected to size exclusion chromatography using a Superdex 200 column (GE HealthCare). Finally, protein samples were concentrated to a final concentration of ~3 mg/ml by using Centricon filters (Millipore), aliquoted and flash-frozen in liquid nitrogen for -80ºC storage. The His-VP3 FL, His-VP3 ΔCt and His-VP3 FL $R_{200}D$ fusion proteins obtained from Baculoviruses were used for co-flotation, bio-layer interferometry and cryo-EM assays.

For His-2xFYVE polypeptide production, *E. coli* BL21 DE3 cells containing the plasmid pET32a(+)-2xFYVE were grown at 37°C until an OD600 of 0.6 was reached. Protein expression was induced

overnight at 18°C using 1mM IPTG. Cells were harvested via centrifugation, resuspended in buffer [10 mM TRIS-HCl (pH 8.0), 100 mM NaCl] supplemented with protease inhibitors and sonicated. The cell lysate was clarified via centrifugation at 18.000 g for 20 min at 4°C and the resulting supernatant was subjected to IMAC purification by using a Ni^{2+} affinity column (HiTrap Fast Flow Crude, GE Healthcare). Resin-bound proteins were eluted with elution buffer [10 mM TRIS-HCl (pH 8.0), 100 mM NaCl, 500 mM imidazole]. His-2xFYVE-containing fractions were pooled and subjected to size exclusion chromatography using a Superdex 75 column (GE HealthCare). Finally, protein samples were concentrated to a final concentration of ~3 mg/ml by using Centricon filters (Millipore), aliquoted and flash-frozen in liquid nitrogen for -80ºC storage. The His-2xFYVE was used as a positive control in co-flotation, bio-layer interferometry and cryo-EM assays.

For GST-2xFYVE polypeptide production, a classical GST fusion protein purification protocol, using pGEX-5X-1 vector (GE Healthcare, 27-4584-01) cloning as described was followed (Nascimbeni et al., 2017). Briefly, *E. coli* BL21 DE3 strain maxi-cultures were lysed and subjected to glutathione beads binding for GST purification. The glutathione beads were finally treated with benzamidine-coated beads (GE Healthcare Life Science, 17512301) to remove the factor Xa and dialyzed for the final purification in a 75 mM Kac, 30 mM HEPES, pH 7.4, 5 mM $MgCl_2$ solution. The GST-2xFYVE fusion protein was used as a probe to detect PI3P in immunofluorescence assays.

Purified proteins quantification and quality control assessment. His-VP3 FL, VP3 ΔCt, VP3 FL $R_{200}D$, and His-2xFYVE quantification at 280 nm was carried out by recording a full spectrum between 240 and 340 nm. Measurements were done with 60 µL of buffer and sample at 20°C in a 1 cm quartz cell, reference 105.202-QS.10 (Hellma Analytics, France), using a JASCO V-750 spectrophotometer (JASCO Corporation, Japan). A baseline subtraction at 340 nm was performed with the Spectragryph

software to accurately calculate the protein concentration. The assessment of the sample homogeneity was performed by Dynamic Light Scattering (DLS) analysis on a DynaPro Plate Reader III (Wyatt, Santa Barbara, CA, USA) to ensure that the samples did not contain aggregates. A volume of 20 µL of sample was loaded in a 384-well microplate (Corning ref 3540, New-York, USA), with 10 acquisitions of 5 s each at 20°C, monitored with the DYNAMICS version V7.10.0.21 software (Wyatt, Santa Barbara, CA, USA), three repetitions per measurement. Finally, the protein integrity and purity were assessed by intact mass spectrometry on a Bruker UltrafeXtreme MALDI-TOF/TOF instrument. A volume of 15 µL of protein was passed through a ZipTip C4 and eluted on a MTP 384 ground steel target plate (Bruker-Daltonics, Germany) with 2 µl of a 20 mg/ml α-Cyano-4-hydroxycinnamic acid in 50% acetonitrile, 0.1% trifluoroacetic acid as matrix solution. Data were acquired using Flexcontrol software (Bruker-Daltonics, Germany) and shots were recorded in positive ion linear mode. Mass spectra were externally calibrated in the m/z range of 15-60 kDa with the Protein II (Bruker-Daltonics, Germany) and analyzed with the flexAnalysis software (Bruker).

Liposome preparation. Liposomes were freshly prepared by the freeze-thaw and extrusion method (F Olson, C A Hunt and W J Vail, 1979). Briefly, lipids dissolved in chloroform were mixed and placed in glass vials, and the chloroform was evaporated by centrifuging 2 h at 35ºC in a SpeedVac. The dried lipids were resuspended in a binding buffer composed of 150 mM NaCl, 20 mM Tris-HCl, pH 8 to a final concentration of 5 mM. The preparation was submitted to ten cycles of freezing in liquid nitrogen and thawing in a 37°C water bath. To generate small unilamellar liposomes, the multilamellar lipids were extruded through polycarbonate membranes (pore size 200 nm, Whatman). The liposomes were used within 1 week. The lipids POPE (1-palmitoyl-2-oleoyl-sn-glycero-3-phosphoethanolamine), POPC (1-palmitoyl-2-oleoyl-sn-glycero-3-phosphocholine), PI3P [1,2-dioleoyl-sn-glycero-3-phospho’(1'-myo-

inosito'-3'-phosphate)], PA (1,2-dioleoyl-sn-glycero-3-phosphate) and PI [1,2-dioleoyl-sn-glycero-3-phospho'(1'-myo-inositol)] were purchased from Avanti Polar Lipids. Liposomes PI3P(-) liposomes were prepared as a mixture of POPE and POPC at a molar ratio of 64:36. Liposomes PI3P(+), PA(+) or PI(+) were prepared as a mixture of POPE and POPC, with either PI3P, PA or PI at a molar ratio of 64:31:5.

Liposome co-flotation assay. For liposome co-flotation assays, the following proteins were used: His-VP3 FL, VP3 ΔCt, VP3 FL $R_{200}D$ produced in the Bac-to-Bac™ Baculovirus Expression System (Invitrogen), and His-2xFYVE produced using the *Escherichia coli* prokaryotic system. Then, 3 mM liposomes were incubated with 1 μM protein in binding buffer composed of 150 mM NaCl, 20 mM Tris-HCl, pH 8 at 4ºC overnight (on), in a final volume of 100 μl. Liposomes and liposome-protein complexes were separated from unbound protein by ultracentrifugation of the reaction mixture in 5 mL Optiprep™ (Axis-Shield PoC AS) density gradients for 1 hour at 40,000 ×g (SW55Ti Beckman Coulter rotor). The liposome-protein mixture was adjusted to 34% Optiprep concentration in a volume of 300 μl, and loaded onto the bottom of the tube that contained 4.5 ml of 20% Optiprep in 150 mM NaCl, 20 mM Tris-HCl, pH 8, overlaid with 200 μl of the buffer. The three top and the bottom fractions, containing 400 μl of the gradient were used for SDS-PAGE gel analysis and immunoblotting against His-tag and anti-VP3 rabbit polyclonal serum.

Cryo-electron microscopy. Protein-liposome complexes were prepared as described for co-flotation assays. Then, 4 μl of the samples were spotted on glow-discharged lacey grids (S166-3, EMS) and cryo-fixed by plunge freezing at -180°C in liquid ethane using a Leica EMGP (Leica, Austria). Grids were observed with a Tecnai F20 electron microscope (Thermo Fisher Scientific). The Tecnai F20 was

operated at 200 kV and images were acquired under low-dose conditions using the software EPU (Thermo Fisher Scientific) and a direct detector Falcon II (Thermo Fisher Scientific). For immunogold staining, the purified protein were first incubated with 5 µL of Ni-NTA [nickel (II) nitrilotriacetic acid] gold particles 0.5 mM in a five times gold particles/purified protein proportion in binding buffer to a final volume of 10 µl. This reagent comprises 5 nm gold particles covered with multiple Ni-NTA functionalities incorporated into the ligands on the surface of gold particles. Each Ni^{2+} coordinates with one NTA and two histidines from the His-tagged recombinant protein to form a stable complex with extremely low dissociation constants (Reddy et al., 2005). Then, 4 µl of this mix were incubated with 6 µl of 3 mM liposome preparation on at 4ºC. Finally, 4 µl of each complex was subjected to cryo-fixation and cryo-EM analyzed as mentioned.

Bio-layer interferometry (BLI) assays. His-2xFYVE, His-VP3 FL or His-VP3 ΔCt were immobilized on Octet NTA biosensor (Sartorius) incubated in an Octet^{Red} 384 system (ForteBio). The functionalized sensors were then washed for 120 s in binding buffer composed of 150 mM NaCl, 20 mM Tris-HCl, pH 8 - BSA (1 mg/mL) before dipping for 600 s into solutions of liposomes diluted in binding buffer - BSA to a final concentration of 5.0, 1.5 or 0.5 mM. Dissociation of the liposome/protein complexes was then monitored in binding buffer - BSA for 300 s. All the experiments were performed in duplicate on two different sensors to account for potential experimental artifacts due to inter-sensor variability. In all cases, potential non-specific interactions were monitored using a sensor coated with the fusion His-Streptavidin as a negative control. The curves were processed using BiaEvaluation software (Biacore).

Recombinant mammalian expression plasmids. Plasmids encoding EGFP-Rab5 was kindly provided by Philip D. Stahl (Washington University, St. Louis, MO) to our group. Plasmids pcDNA VP3 FL and

pcDNA VP3 P2 (P2 all reversed) were constructed by Valli and collaborators in a previous study (Valli et al., 2012) and kindly provided by José F. Rodríguez (CSIC, Madrid, Spain) to our group. The plasmids encoding point mutant VP3 proteins ($K_{157}D$, $R_{159}D$, $H_{198}D$ and $R_{200}D$) were obtained by site-directed mutagenesis. For this purpose, the plasmid pcDNA VP3 FL was used as template DNA in polymerase chain reactions (PCR) together with oligonucleotide primer pairs containing changed nucleotides in order to generate the point mutations (*SI Appendix*, Table 1). PCRs were carried out using Pfu DNA polymerase (PB-L, Argentina) and the following conditions: initial DNA denaturation at 95ºC for 5 min followed by 30 cycles of 95ºC for 1 min, 65ºC for 1 min and 72ºC for 6 min and a final extension at 72ºC for 10 min. The size of the amplified products was corroborated by agarose gel electrophoresis. In order to degrade the plasmid mold, the PCR mixtures were incubated with *Dpn*I endonuclease (ThermoFisher Scientific, USA) at 37ºC for 2 h followed by heating at 80ºC for 20 min. Aliquots of those reactions were transformed into competent *E. coli* DH10B cells (Invitrogen, USA). Colonies carrying the mutated plasmids were selected in LB plates containing ampicillin (100 µg/mL). Plasmids were purified using the EasyPure® Plasmid MiniPrep Kit (TransGen Biotech Co., Ltd, China) and the introduction of mutations was confirmed by nucleotide sequencing (Macrogen service, South Korea). Alignments and prediction of amino acid sequences were performed using the Aligner and Translator tools from the JustBio website ("JustBio," n.d.).

Transient transfections and indirect immunofluorescence assay. QM7 cells were grown on coverslips in an M24 multi-well plate for 12 h to approximately 70% confluence and then plasmids were transfected employing Lipofectamine 3000 (number L300015; Thermo Fisher, Argentina) following the manufacturer's recommendations. After 24 h p.i., the cells were fixed with 4% paraformaldehyde (PFA) for 15 min at room temperature (RT), washed with PBS (pH 7.4), and permeabilized with 0.05% saponin

in PBS containing 0.2% BSA for 20 min at RT. Then the cells were incubated with anti-VP3 primary antibodies overnight (ON) at 4ºC in a humidity chamber, and after extensive washing, cells were incubated with secondary antibodies conjugated with Alexa Fluor Cy3 for 1 h 30 min, followed by extensive washes in PBS. The coverslips were mounted in Mowiol plus Hoechst and analyzed by Confocal Laser Scanning Microscopy (CLSM). Images were captured using an Olympus FluoView TM FV1000 confocal microscope (Olympus, Argentina) with FV10-ASW (version 01.07.00.16) software and processed using the ImageJ software (Schindelin et al., 2012). For quantification of VP3 cellular distribution (Fig. 2D), the percentage of cells with vesicular distribution of the red signal was calculated out of approximately 30 cells per construct and experiment. For quantification of the co-localization of VP3 and either EGFP-Rab5 or EGFP-2xFYVE, the Manders M_2 coefficient was calculated out of approximately 30 cells per construct and experiment (*SI Appendix*, Fig. S3 and Fig. 3A, respectively). The M2 coefficient, which reflects co-localization of signals, is defined as the ratio of the total intensities of magenta image pixels for which the intensity in the blue channel is above zero to the total intensity in the magenta channel. JACoP plugin was utilized to determine M2 (Bolte and Cordelières, 2006). For VP3 puncta co-distributing with EEA1 and GST-2xFYVE the number of puncta co-distributing for the three signals was manually determined out of approximately 40 cells per construct and experiment per 200 μm^2 (Fig. 3B).

Reverse genetics. For the generation of recombinant IBDV we used a modification of the reverse genetics system described by Qi and coworkers (Qi et al., 2007), in which the full-length sequences of the IBDV segments, flanked by a hammerhead ribozyme at the 5'-end and a hepatitis delta ribozyme at the 3'-end, are expressed under the control of an RNA polymerase II promoter. For its construction, the complete segments of IBDV Soroa were amplified from viral dsRNA using a sequence independent

amplification method (Potgieter et al., 2009) and cloned in plasmid pJET1.2 (Thermo Fisher Scientific). The hammerhead ribozymes, specific for each segment, are based in the HamRz-R, described by Yanay and cols. (Yanai et al., 2006), with 10 nucleotides of sequence complementary to each IBDV segment stabilizing Stem I. At the 3'-end, we used the sequence of the antigenomic hepatitis delta ribozyme HDVagrz SC (Ghanem et al., 2011). DNA fragments containing the ribozyme sequences were constructed by PCR-based gene synthesis with oligonucleotides designed by the Assembly PCR Oligo Maker software (Rydzanicz et al., 2005). Each PCR-amplified IBDV full-length segment were cloned, flanked by the corresponding hammerhead ribozyme and HDVagrz SC, between the *Eco*RI and *Not*I sites of plasmid pCAGEN [a gift from Connie Cepko; Addgene plasmid # 11160; (Matsuda and Cepko, 2004a)] by Gibson assembly (Gibson et al., 2009). The correctness of the sequences in both plasmids, pCAGEN.Hmz.SegA.Hdz (SegA) and pCAGEN.Hmz.SegB.Hdz (SegB), was assessed by sequencing (Eurofins Scientific). The plasmid pCAGEN.Hmz.SegA.R_{200}D.Hdz (SegA.R_{200}D) was purchased to GenScript and the mutation was verified by sequencing of the complete plasmid (Eurofins Scientific).

Recombinant viruses foci forming units assay. QM7 cells were grown in M24 multi-well plates for 12 h to approximately 90-95% confluency and then 800 ng (400 ng of plasmid with each segment) were transfected by using Lipofectamine 2000 (number 11668027; Thermo Fisher, Spain) following the manufacturer's recommendations. When performing single segment transfections (SegA, SegB and SegA.R_{200}D), 400 ng of the plasmid pCAGIG (a gift from Connie Cepko; Addgene plasmid #11159; (Matsuda and Cepko, 2004b) was added to 400 ng of those containing the viral segments to reach a total of 800 ng of total DNA per transfection. pCAGIG is a mammalian expression vector that shares the backbone with the pCAGEN vector used for the expression of the viral segments. The following transfections were performed in triplicate: SegA, SegB, SegA.R_{200}D, SegA+SegB or SegA.R_{200}D+ SegB.

At 8 h post-transfection (p.t.) the supernatants were discarded and the monolayers were recovered for further plating on M6 multi-well plates containing non transfected QM7 cells. For monolayers transfected with SegA, SegB, SegA.R_{200}D and SegA.R_{200}D+ SegB half of the transfected monolayer was plated on fresh cells. For SegA+SegB, which leads to the production of wild type virus, several dilutions were tested, always in triplicate. To limit virus diffusion and facilitating the foci forming Avicel RC-591 (FMC Biopolymer) was added to the M6 multi-well plates. 72 h p.i., the monolayers were 16% formaldehyde-fixated and stained with Coomassie R250 (BioRad).

Statistical analysis. One-way ANOVA followed by a Tukey's HSD (honestly significant difference) test were performed using AnalystSoft Inc., StatPlus:mac - Version v8 ("AnalystSoft Inc., StatPlus:mac - v8," n.d.). Plotting was done using the *ggplot2* package (Wickham, 2016) in R, with assistance from the RStudio software (RStudio Team, 2020).

Bioinformatics analysis. Multiple sequence alignment and the percent identity matrix were performed with Clustal OMEGA (v1.2.4) (Sievers et al., 2011) implemented at EMBL's European Bioinformatics Institute ("EMBL's European Bioinformatics Institute," n.d.). Accession numbers of the sequences: Infectious bursal disease virus (AF_140705.1); Blotched snakehead virus (YP_052872.1); Victorian trout aquabirnavirus (YP_009255397.1); Tellina virus 2 (YP_010084301.1); Yellowtail ascites virus (NP_690805.1); Infectious pancreatic necrosis virus (NP_047196.1); Tasmanian aquabirnavirus (YP_009177608.1); Lates calcarifer birnavirus (YP_010086267.1) and Tellina virus 1 (YP_009509080.1). Alignment visualization was done with the R *ggmsa* package (Zhou et al., 2022) with the assistance from the RStudio software (RStudio Team, 2020). Amino acids are colored according

to their side-chain chemistry. Protein sequence logos annotation is displayed on top of the amino acid alignment.

The model of VP3 FL from IBDV ([strain Soroa, GenBank AF140705.1, residues 756-1012 (257 residues) from the polyprotein] was generated using a local copy of AlphaFold-2 (Jumper et al., 2021), installed using the open-source code available at https://github.com/deepmind/alphafold (accessed on 1 September 2021). Runs were performed on a Centos 7 workstation with 64 CPUs and 4 GeForce RTX 2080 Ti GPUs, using the casp14 preset and including all PDB templates present in the database. The program produces a per-residue confidence metric termed pLDTT on a scale from 0 to 100. pLDTT values higher than 70 reflect reliable models with correct backbone predictions, and those with values higher than 90 correspond to models with both reliable backbone and side-chain orientation predictions. pLDTT values lower than 50 are a strong predictor of disorder, and regions with such values are either unstructured under physiological conditions or only structured as part of a complex.

Reagents and antibodies. Western blot and confocal laser scanning microscopy (CLSM) analyses were carried out using rabbit anti-VP3 specific sera followed by horseradish peroxidase (HRP)-conjugated anti-rabbit secondary antibodies (number A0545), purchased from Sigma-Aldrich (Buenos Aires, Argentina). For early endosomes detection by CLSM, we used anti-EEA1 mouse monoclonal antibody (1:200 dilution; BD Transduction Laboratories, 610456), and for anti-GST detection, we used Alexa Fluor 649-labelled goat anti-GST (Rockland-Inc, 600-143-200). Fluorescently labelled secondary antibodies, all diluted 1:200 from Invitrogen, included Alexa Fluor 546 donkey anti-mouse (A10036), and Alexa Fluor 546 donkey anti-rabbit (A10040).

Far-UV circular dichroism (CD) of VP3 proteins. His-VP3 FL and His-VP3 FL $R_{200}D$ at a concentration of 2 mg/ml in 50 mM Tris-HCl pH 8, 500 mM NaCl were analysed by far-UV CD (180-260 nm). CD spectra were obtained with an AVIV CD spectropolarimeter model 215 using a 0.02 cm path length cell at RT. Five successive scans were averaged and the background spectrum of the sample buffer, acquired under identical conditions, was subtracted. The resulting corrected CD intensities were then converted to $\Delta\varepsilon$ per residue. Secondary structure contents were estimated from the far-UV CD spectra using the CDSSTR routine (Johnson, 1999) of the DICHROWEB server (Whitmore and Wallace, 2008, 2004) run on the SP175 reference dataset (Lees et al., 2006), containing 72 proteins representing a large panel of secondary structures. Similar results were obtained on different datasets (Sreerama and Woody, 2000) or by using the CONTIN/LL routine (Provencher and Glöckner, 1981).

Coarse Grain (CG) models of VP3 constructs. Three main protein constructs derived from VP3 were considered: 1. VP3 Ct. A peptide comprising the last 36 residues of VP3 (223 to 257). VP3 Ct has an overall electrical charge of +5, and is absent from the available crystal structure of VP3. Consequently, it was assumed to be a disordered domain and was modeled as unstructured. 2. VP3 ΔNt. A shorter version of VP3 that lacks the first 81 residues leading to the Nt. It consists of the crystallized structure of the protein core (residues 82 to 222, available from the Protein Data Bank PDB ID 2R18), concatenated with the VP3 Ct peptide. As the first 9 residues of the protein core are also missing from resolved structure, they were modeled as unstructured, similar to the VP3 Ct fragment. VP3 ΔNt was selected primarily because it contains the structural information of the crystallized protein, which provides valuable insights into the protein's overall structure and function. In addition, the construct includes the Ct peptide (VP3 Ct), which is crucial for membrane binding. Although the Nt 81 residues are absent in this construct, their exclusion was found to be inconsequential in terms of evaluating the

protein's binding energy and positioning on the membrane surface (compare, for example, VP3 ΔNt and VP3 FL in Figure 5). 3. VP3 FL. The full-length VP3 protein, which was obtained as an AlphaFold2 prediction (Jumper et al., 2021). The structure of the protein predicted by AlphaFold2 not only provided insight into the overall architecture of VP3, but it also reinforced our model of unstructured VP3 Ct. It is worth noting that the Nt 81 residues, which are absent in VP3 ΔNt, are predicted to be in a modular conformation, constituting a globular domain separated by a loop from the globular domain of the core region (crystallized residues 82 to 222). The structural information provided by the full-length VP3 model is therefore useful in understanding the interaction with lipid membranes. In addition to VP3 Ct, VP3 ΔNt, and VP3 FL, two mutants of VP3 ΔNt were simulated: VP3 ΔNt $R_{200}D$, in which R_{200} was replaced by aspartate (D), and VP3 ΔNt P2 Mut, where the whole P2 region (R_{200}, H_{198}, R_{159}, and K_{157}) was replaced by D. All proteins were modeled with the MARTINI force-field (De Jong et al., 2013) [whenever needed, the secondary structure of the non-disordered protein domains was restrained by means of the ElNeDyn elastic network model (elnedyn22)] (Periole et al., 2009; Poma et al., 2017). In this case, harmonic potentials with a force constant of 1000 kJ mol^{-1} nm^2 were applied between backbone particles separated by less than 1.4 nm. In the construction of VP3 ΔNt, elastic network restrictions were applied to residues 91 to 220, which was the fragment resolved from by crystallography. However, in VP3 FL, the elastic network was applied to all globular domains, while leaving the linkers and the last 36 residues at the Ct unrestricted.

Molecular Theory calculations. The Molecular Theory (MT) used to assess protein adsorption is detailed in references (Chiarpotti et al., 2021; Ramírez et al., 2019). Briefly, this mean-field method yields the distribution of macromolecules in an anisotropic system, through the minimization of a model free-energy functional that accounts for electrostatic and steric interactions, the configurational and

translational entropy of the macromolecules, the translational entropy of the free species (protons, hydroxyls, and salt ions) and the acid-base equilibrium of all ionizable molecules in the system. In the present case, the membrane was modeled as a dielectric slab of thickness h, with a dielectric constant ε_M, which is in contact with a solution of dielectric constant ε_S. Far from the membrane ($z \rightarrow \infty$), the solution is in contact with an infinite bulk that contains the proteins (1 μM concentration), all the free species, and a fixed pH=8. The rigid membrane contained 15% of ionizable groups on its surface, in order to mimic the 5% of ternary ionizable PI3P. One third of these groups were assigned a pK_a of 2.5, corresponding to the phosphate group of the glycerol moiety, while the pK_a for the rest was set to 6.5, corresponding to the phosphoesther groups of inositol. MT requires the input of a large set of protein conformations, which are subsequently reweighted by the theory. These conformations were generated by Molecular Dynamics simulations of the proteins in water. VP3 Ct, VP3 ΔNt, VP3 FL, VP3 ΔNt $R_{200}D$, and VP3 ΔNt P2 Mut, were modeled using MARTINI-2.2 parameters (Marrink et al., 2007). The proteins were hydrated in MARTINI polarizable water. As stated before, the proteins globular segments (residues 92-222 in VP3 FL, VP3 ΔNt and its mutants, and residues 7-79 additionally in VP3 FL) were restricted through the application of the elastic network ElNeDyn (Marrink et al., 2007) with a spring constant of 1000 $kJ.mol^{-1}$ applied to backbone beads (BB) within a cutoff distance of 1.4 nm. Each protein was simulated for 100 ns, after equilibration, in the NPT ensemble using GROMACS 2021.3. A cluster analysis was performed in order to obtain the most representative conformations of the simulated ensemble. This method groups conformations by structural similarity, using the root mean squared deviation (RMSD) of the coordinates calculated for all conformer pairs along the trajectory, clustering structures with RMSD $\leq$ 0.3 nm. This procedure leads to 50 conformers for each protein construct. Each conformer was subsequently rotated 30 times randomly to produce a set of 1500 configurations for the MT calculations.

Molecular Dynamics Simulations of VP3 on a lipid bilayer. MARTINI-2.2 was also used to model the lipid molecules in our MD simulations. The bilayer was assembled using insane utility (Wassenaar et al., 2015), while hydration with polarizable water molecules and ions was performed with the solvate utility of the GROMACS package. The bilayer had a symmetric lipid composition of 30% 1,2-dioleoyl-sn-glycero-3-phosphocholine (DOPC), 65% of 1,2-dioleoyl-sn-glycero-3-phosphoethanolamine (DOPE) and 5% 1,2-dioleoyl-sn-glycero-3-phosphatidylinositol-3-phosphate (PI3P), leading to a lipid composition of 111:231:18 (DOPC, DOPE, and PI3P) in each leaflet. The protein was placed at a distance of 10 nm from the membrane surface, to avoid a possible initial binding bias. The system was then equilibrated and finally simulated for 500 ns. Both equilibration and production were in the NPT ensemble. A semi-isotropic Parinello-Rahman barostat (Parrinello and Rahman, 1981) with a 12 ps time constant, and lateral and normal compressibilities of 3×10^{-4} bar^{-1} were used to keep the pressure at 1.0 bar. The v-rescale thermostat, with a time constant of 1 ps, was used to keep the temperature at 325 K. In all cases the integration timestep was 20 fs. Long range electrostatics were calculated using the particle mesh Ewald (PME) method (Darden et al., 1993) with a real-space cut-off of 1.2 nm.

Acknowledgments

This project was partially supported by: the National Agency for Scientific and Technological Promotion, Ministry of Science, Technology and Innovation, through grants PICT 2016-0528 and 2019-01324 to L.R.D; PICT 2015-2210 to F.A.Z; PICT 2019-01889 to L.M.P. and PICT 2020-3795 to M.G.D.P; the National Scientific and Technical Research Council through grants PIP 2015-2017 11220150100114CO and 2021-2023 11220200103139CO to L.R.D.; 2021-2023 11220200103195CO to L.M.P. and 11220200103223CO to M.G.D.P.; and by the National University of Cuyo through grants 2013-2015

M006, 2016-2018 M029, 2019-2021 M071 and 2022-2024 M012 to L.R.D. For stays performed by L.R.D. in the laboratory of Structural Virology at the Institut Pasteur in Paris, we are grateful for the support of National University of Cuyo through the Teaching Staff Mobility Program in 2018-2019, the Ministry of Education through the Program scholarships for training abroad in Science and Technology (BEC.AR 2018), and the International Union of Biochemistry and Molecular Biology (IUBMB) through a "2020 Mid-Career Research Fellowship". The work in Madrid was supported by grants from the Spanish Ministry of Science and Innovation (PID2020-113287RB-I00) and the Comunidad Autónoma de Madrid (P2018/NMT-4389) to JRC. At the IHEM, we sincerely appreciate Elisa Bocanegra, Norberto Domizio, and Jorge Ibañez for valuable technical assistance in CLSM handling. At the Institut Pasteur in Paris, we are grateful to Gérard Pehau-Arnaudet and the staff at the Ultrastructural BioImaging core facility for image acquisition and analysis; to Patrick England and Sébastien Brûlé and the staff of the Molecular Biophysics platform for purified protein analyses, CD and BLI assays, to Stéphane Petres and members at the Production and Purification of Recombinant Proteins Technological Platform, and to the staff of the Proteomics platform.

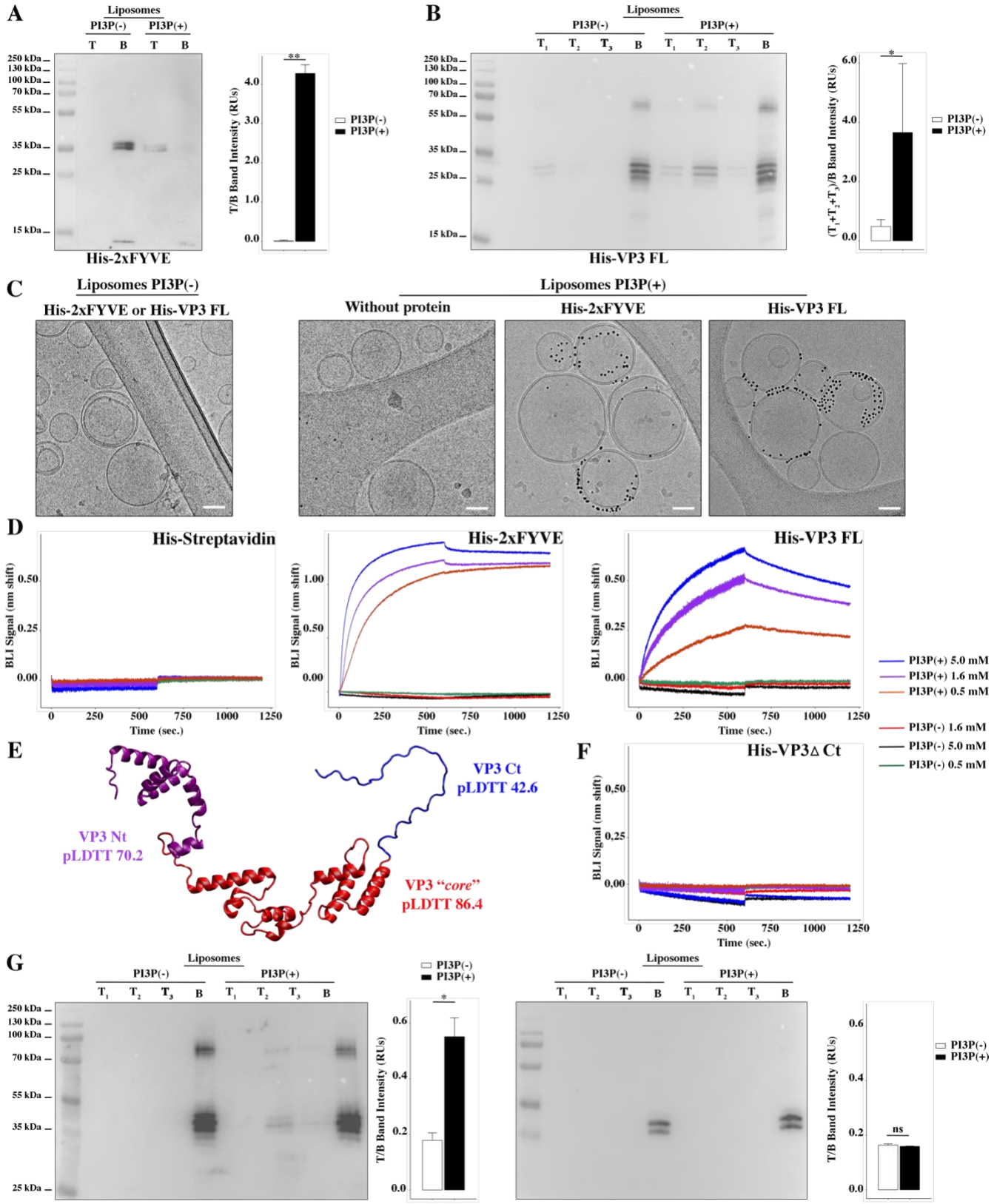
A
Liposomes
PI3P(-)
PI3P(+)
T B T B
250 kDa
130 kDa
100 kDa
70 kDa
55 kDa
35 kDa
25 kDa
15 kDa
His-2xFYVE
T/B Band Intensity (RUs)
PI3P(-)
PI3P(+)
B
Liposomes
PI3P(-)
PI3P(+)
T1 T2 T3 B T1 T2 T3 B
His-VP3 FL
(T1+T2+T3)/B Band Intensity (RUs)
C
Liposomes PI3P(-)
His-2xFYVE or His-VP3 FL
Liposomes PI3P(+)
Without protein
His-2xFYVE
His-VP3 FL
D
His-Streptavidin
His-2xFYVE
His-VP3 FL
BLI Signal (nm shift)
Time (sec.)
PI3P(+) 5.0 mM
PI3P(+) 1.6 mM
PI3P(+) 0.5 mM
PI3P(-) 1.6 mM
PI3P(-) 5.0 mM
PI3P(-) 0.5 mM
E
VP3 Ct
pLDTT 42.6
VP3 Nt
pLDTT 70.2
VP3 "core"
pLDTT 86.4
F
His-VP3Δ Ct
BLI Signal (nm shift)
Time (sec.)
G
Liposomes
PI3P(-)
PI3P(+)
T1 T2 T3 B T1 T2 T3 B
250 kDa
130 kDa
100 kDa
70 kDa
55 kDa
35 kDa
25 kDa
T/B Band Intensity (RUs)
ns

747

Figure 1. Biophysical characterization of VP3 binding to PI3P.

(A) Immunoblots of the top (T) and bottom (B) fractions from a liposome PI3P(-) or PI3P(+) OptiprepTM co-floatation assay indicating that His-2xFYVE protein (~35 kDa) specifically binds to liposome PI3P(+). Results are representative of three independent experiments. The bar plot represents the intensity of T/B bands for each liposome preparation. Significant differences (** P <0.01) as determined by one-way ANOVA with Tukey's HSD test.

(B) Immunoblots of the three top (T_1, T_2 and T_3) and bottom (B) fractions from a liposome PI3P(-) or PI3P(+) OptiprepTM co-floatation assay indicating that His-VP3 FL protein (~32 kDa) specifically binds to liposome PI3P(+). Results are representative of three independent experiments. The bar plot represents the intensity of (T_1+T_2+T_3)/B bands for each liposome preparation. Significant differences (* P <0.05) as determined by one-way ANOVA with Tukey's HSD test.

(C) Liposomes were vitrified and only representative cryo-electron microscopy images are shown. Left panel: liposomes PI3P(-) incubated even with the Ni-NTA gold particles reagent alone or pre-incubated with His-2xFYVE of His-VP3 FL. Right panel: liposomes PI3P(+) control (without protein), or incubated with His-2xFYVE- or His-VP3 FL-Ni-NTA gold particles showing gold particles decorating the membrane of the liposomes when His-2xFYVE or His-VP3 FL were present. The bar represents 50 nm.

(D) Binding of His-Streptavidin (negative control), His-2xFYVE (positive control) or His-VP3 FL to three different concentrations of liposomes PI3P(-) or PI3P(+). Association and dissociation sensorgrams measured by bio-layer interferometry (BLI), showing the specific interaction of His-2xFYVE and His-VP3 FL with liposomes PI3P(+) in a dose-dependent manner, as indicated.

(E) Cartoon representation of AlphaFold2 prediction of VP3 FL. Red region corresponds to the "*core*" region of the protein present in the experimental X-ray crystallographic model obtained by Casañas and

coworkers [PDB: 2R18 (Casañas et al., 2008)]. Regions not present within the PDB are colored in violet and blue representing the Nt and the Ct of VP3, respectively. pLDTT values lower than 50 are a strong predictor of disorder.

(F) Binding of His-VP3 ΔCt to three different concentrations of liposomes PI3P(-) or PI3P(+). Sensorgrams measured by BLI, showing the absence of binding to either liposomes when the VP3 lacks the Ct region [blue in (E)].

(G) Immunoblots of the three top (T_1, T_2 and T_3) and bottom (B) fractions from a liposome PI3P(-) or PI3P(+) OptiprepTM co-floatation assay of His-VP3 FL protein (~32 kDa) (positive control, left panel) or His-VP3 ΔCt protein (~28 kDa) (right panel) showing the lack of VP3 ΔCt binding to both liposomes. Results are representative of three independent experiments. The bar plot represents the intensity of (T_1+T_2+T_3)/B bands for each liposome preparation. Significant differences (* P <0.05; ns P >0.05) as determined by one-way ANOVA with Tukey's HSD test.

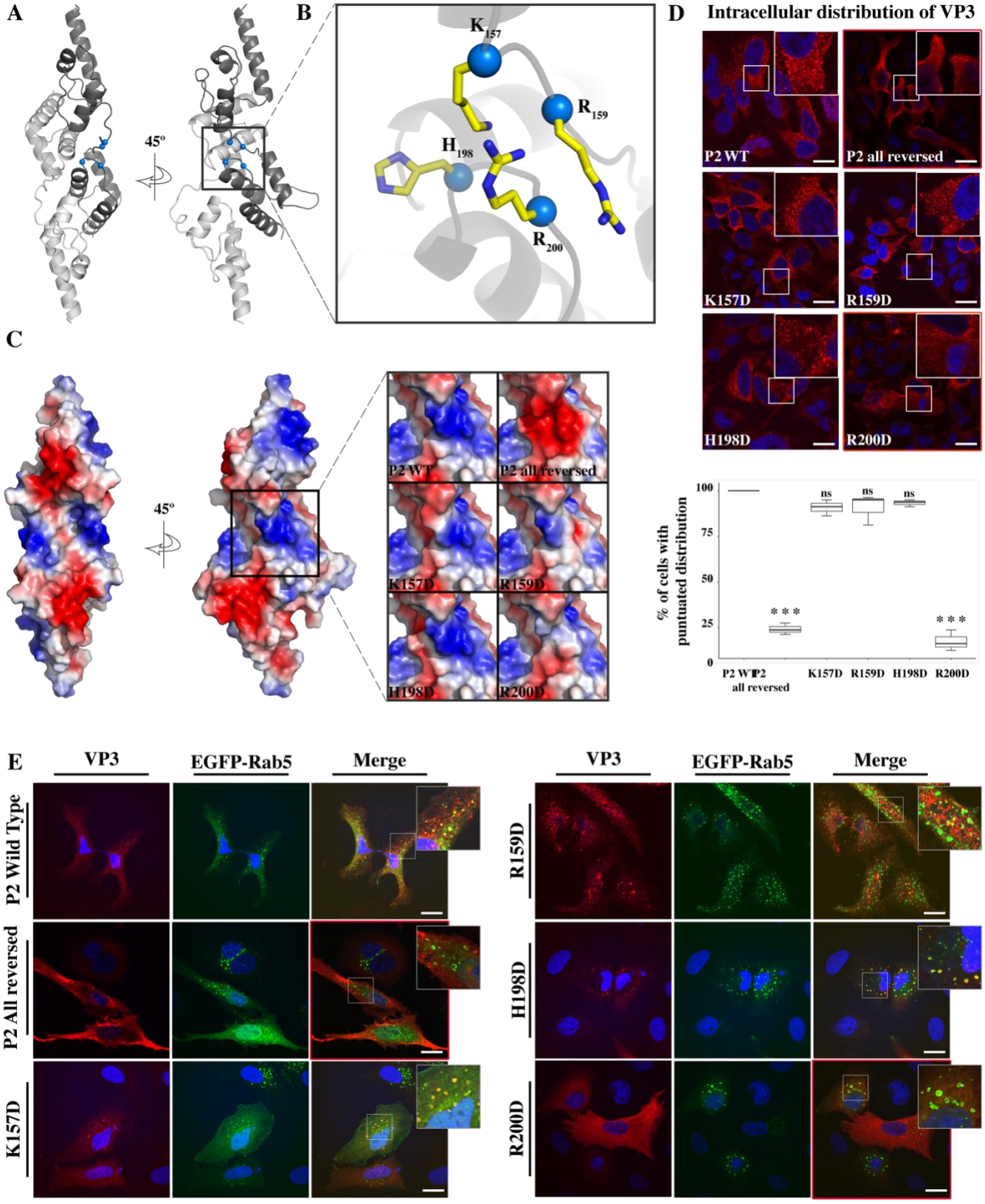
A
45°
B
K157
R159
H198
R200
C
45°
P2 WT
P2 all reversed
K157D
R159D
H198D
R200D
D
Intracellular distribution of VP3
P2 WT
P2 all reversed
K157D
R159D
H198D
R200D
% of cells with puntuated distribution
100
75
50
25
0
ns
ns
ns
* * *
* * *
P2 WT
P2 all reversed
K157D
R159D
H198D
R200D
E
VP3
EGFP-Rab5
Merge
P2 Wild Type
P2 All reversed
K157D
R159D
H198D
R200D

784

Figure 2. VP3 P2 involvement in the association of VP3 with the EE membrane.

(A) The cartoon representation of the VP3 dimer [PDB 2R18 (Casañas et al., 2008)] shows each protomer in different shades of grey. The blue balls depict the residues defining the P2 region.

(B) The close-up of P2 region showing residues K_{157}, R_{159}, H_{198} and R_{200}.

(C) Electrostatic potential mapped on the surface of the structure of a VP3 dimer in the same orientations as in (A) structures. The close-up shows the impact of P2 residue mutations on the electrostatic potential of the binding site. P2 WT corresponds to the "UniProt code". The color-coded electrostatic surface potential of VP3 was drawn using PyMol (blue positive, red negative).

(D) QM7 cells transfected with pcDNA VP3 FL (P2 WT), P2 (all reversed), or the four point mutants ($K_{157}D$, $R_{159}D$, $H_{198}D$ and $R_{200}D$) and immunostained with anti-VP3 showing the distribution of each protein (upper panel). Images were captured using a Confocal Laser Scanning Microscopy and then the percentage of cells with punctated fluorescent signal were determined for each protein (lower panel). The red signal shows the VP3 distribution and the blue one shows the nuclei, which were Hoestch-stained. The data were normalized to the P2 WT protein. The box plot represents the percentage of cells with punctuated distribution of VP3. Significant differences (*** P <0.001; ns P >0.05.) as determined by one-way ANOVA with Tukey's HSD test.

(E) QM7 cells co-transfected with pEGFP-Rab5 and pcDNA VP3 FL (P2 WT), P2 (all reversed), or the four point mutants ($K_{157}D$, $R_{159}D$, $H_{198}D$ and $R_{200}D$) and immunostained with anti-VP3 showing the distribution of each protein. Representative images, captured using a Confocal Laser Scanning Microscopy are shown where green signal represents Rab5 distribution and the red signal that of VP3. Nuclei were Hoestch-stained and are blue. White bar-scales represent 20 μm. VP3 P2 (all reversed) and $R_{200}D$ depict a cytosolic distribution of the proteins. Quantification of the co-localization of the different VP3 proteins and EGFP-Rab5 is shown in *SI Appendix*, Fig. S3.

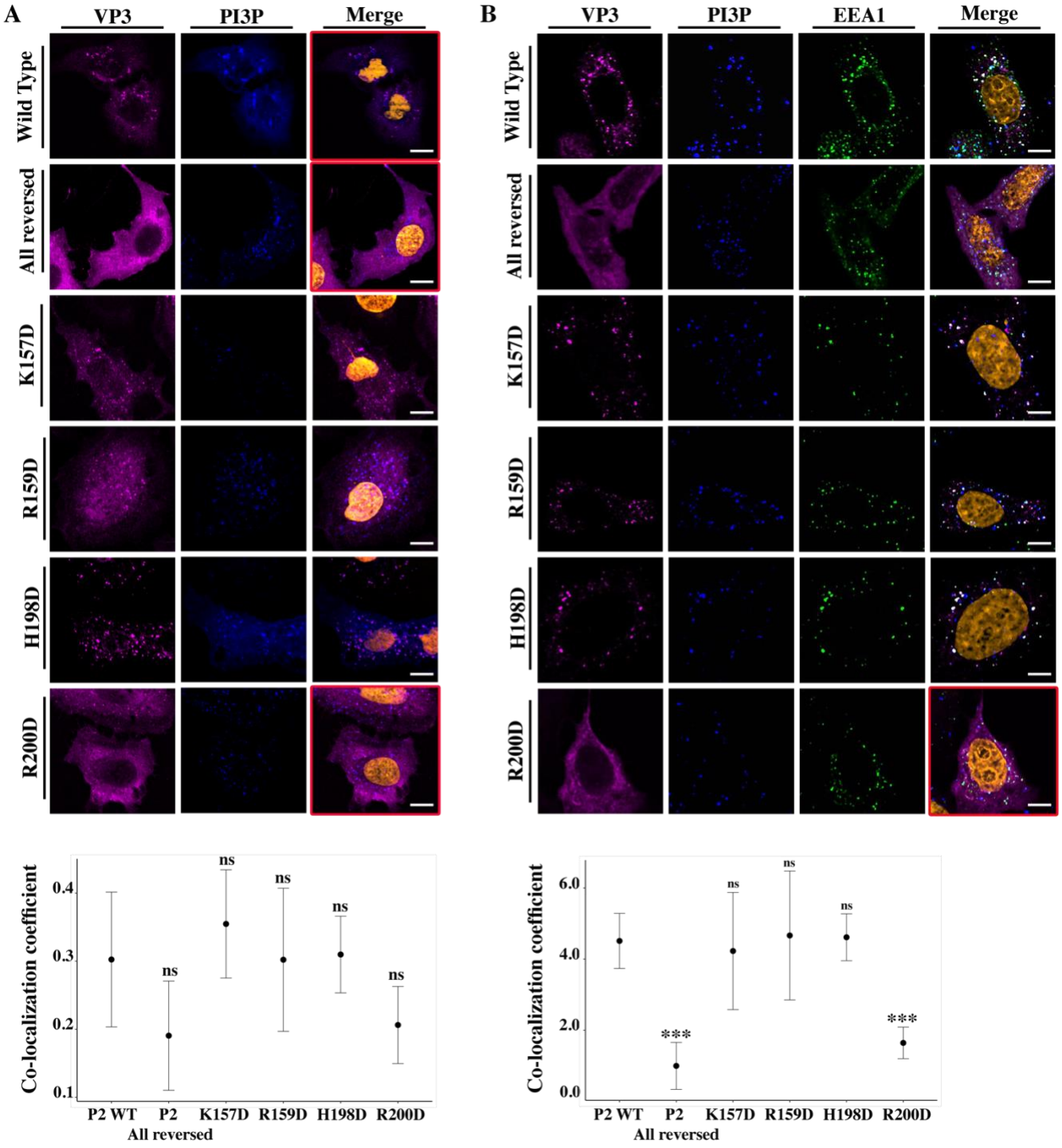

Figure 3. VP3 P2 involvement in the association between VP3 and EE PI3P.

(A) QM7 cells co-transfected with the PI3P biosensor pEGFP-2xFYVE and pcDNA VP3 FL (P2 WT), P2 (all reversed), or the four point mutants ($K_{157}D$, $R_{159}D$, $H_{198}D$ and $R_{200}D$) and immunostained with

anti-VP3 showing the distribution of each protein. Representative images captured using a Confocal Laser Scanning Microscopy are shown where blue signal represents FYVE distribution and the magenta signal that of VP3. Nuclei were Hoestch-stained and are orange (upper panels). White bar-scales represent 20 μm. VP3 P2 (all reversed) and $R_{200}D$ depict a cytosolic distribution of the proteins with a significant lower co-localization coefficient. The dot plot in the lower panel depicts the co-localization coefficient for each protein determined as explained in the Materials and Methods section. Significant differences (ns P >0.05) as determined by one-way ANOVA with Tukey's HSD test.

(B) QM7 cells were transfected with the pcDNA VP3 FL (P2 WT), P2 (all reversed), or the four point mutants ($K_{157}D$, $R_{159}D$, $H_{198}D$ and $R_{200}D$). The cells were fixed and then the GST-2xFYVE purified peptide and anti-VP3 antibodies were used to recognize endogenous PI3P and VP3, respectively. Additionally anti-EEA1 antibodies were used to stain the endosomes. GST-2xFYVE was labelled with a fluorescent anti-GST antibody (blue signal), anti-VP3 and anti-EEA1 antibodies with fluorescent secondary antibodies (magenta and green signals, respectively), and Hoestch-stained nuclei in orange. White bar-scales represent 10 μm. VP3 P2 (all reversed) and $R_{200}D$ depict a cytosolic distribution of the proteins with a significant lower co-localization coefficient. The dot plot in the lower panel depicts the co-localization coefficient for each protein determined as explained in the Materials and Methods section. Significant differences (*** $P < 0.001$; ns P >0.05) as determined by one-way ANOVA with Tukey's HSD test.

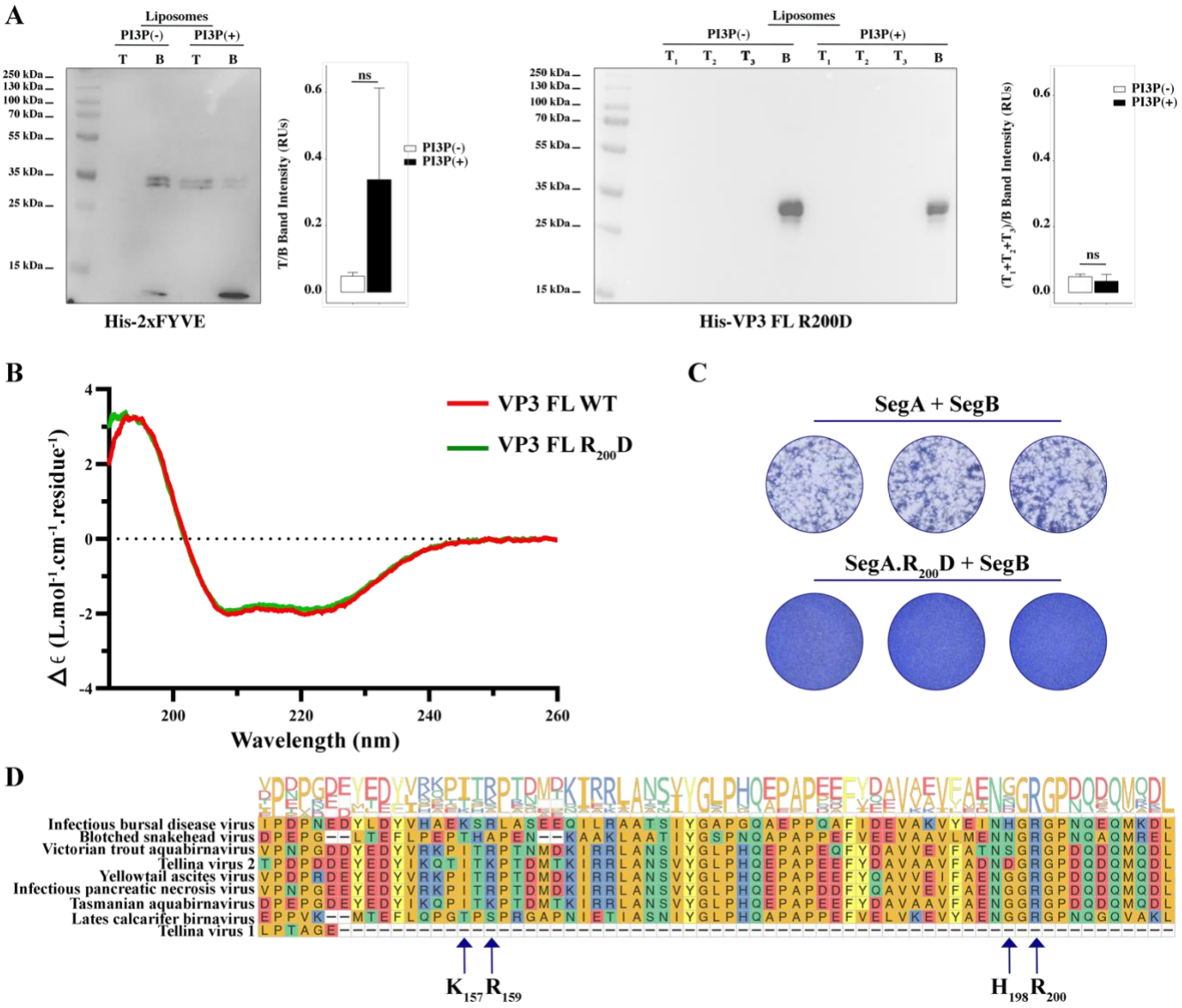

Figure 4. Biophysical characterization of VP3 FL $R_{200}D$ binding to PI3P.

(A, left panel). Immunoblots of the top (T) and bottom (B) fractions from a liposome PI3P(-) or PI3P(+) OptiprepTM co-floatation assay indicating that His-2xFYVE protein (~35 kDa) specifically binds to liposome PI3P(+). The bar plot represents the intensity of T/B bands for each liposome preparation. Significant differences (ns P >0.05) as determined by one-way ANOVA with Tukey's HSD test.

(A, rigth panel). Immunoblots of the three top (T_1, T_2 and T_3) and bottom (B) fractions from a liposome PI3P(-) or PI3P(+) OptiprepTM co-floatation assay indicating that His-VP3 FL $R_{200}D$ protein (~35 kDa)

does not bind to liposome PI3P(-) nor PI3P(+). The bar plot represents the intensity of (T_1+T_2+T_3)/B bands for each liposome preparation. Significant differences (ns P >0.05) as determined by one-way ANOVA with Tukey's HSD test.

(B) Far-UV CD spectra of His-VP3 FL (red line) or His-VP3 FL R_{200}D (green line). Spectral acquisitions at 50 nm/min with 0.1 nm steps at 1 s integration time, with a bandwidth of 1 nm were performed 4 times for the samples as well as for the buffer. The measurements were carried out with constant nitrogen gas flux of 10 ml/min. Acquisitions were averaged and buffer baseline was subtracted with Spectra Manager (JASCO). No smoothing was applied. CDtoolX was used to zero between 255-260 nm and to calibrate the signal amplitude from the fresh CSA signal (Miles and Wallace, 2018). Data are presented as delta epsilon ($\Delta\varepsilon$) per residue ($L.mol^{-1}.cm^{-1}.residue^{1}$) calculated using the molar concentration of protein and number of residues.

(C) QM7 cells were grown in M24 multi-well plate for 12 h to approximately 90-95% confluency and then 800 ng of plasmids were transfected [(SegA + SegB) or (SegA.R_{200}D + SegB)] in triplicate. At 8 h post-transfection (p.t.) the supernatants were discarded, and the monolayers were recovered for further plating on M6 multi-well plates containing non transfected QM7 cells. Avicel RC-591 (FMC Biopolymer) was added to the M6 multi-well plates. 72 h p.i., the monolayers were fixated and stained with Coomassie R250 for revealing the foci forming units.

(D) Partial view of amino acid alignment of the VP3 protein for nine reference members of *Birnaviridae* family. Multiple sequence alignment was performed with Clustal OMEGA (v1.2.4) (Sievers et al., 2011) implemented at EMBL's European Bioinformatics Institute ("EMBL's European Bioinformatics Institute," n.d.) (The complete alignment is shown in *SI Appendix*, Fig. S4A). Alignment visualization was done with the R *ggmsa* package (Zhou et al., 2022) in with assistance from the RStudio software (RStudio Team, 2020). Amino acids are colored according to their side-chain chemistry. Protein

sequence logos annotation is displayed on top of the amino acid alignment. For facilitating the view IBDV VP3 142-210 portion is shown. The black arrow indicates the K_{157}, R_{159}, H_{198} and R_{200}.

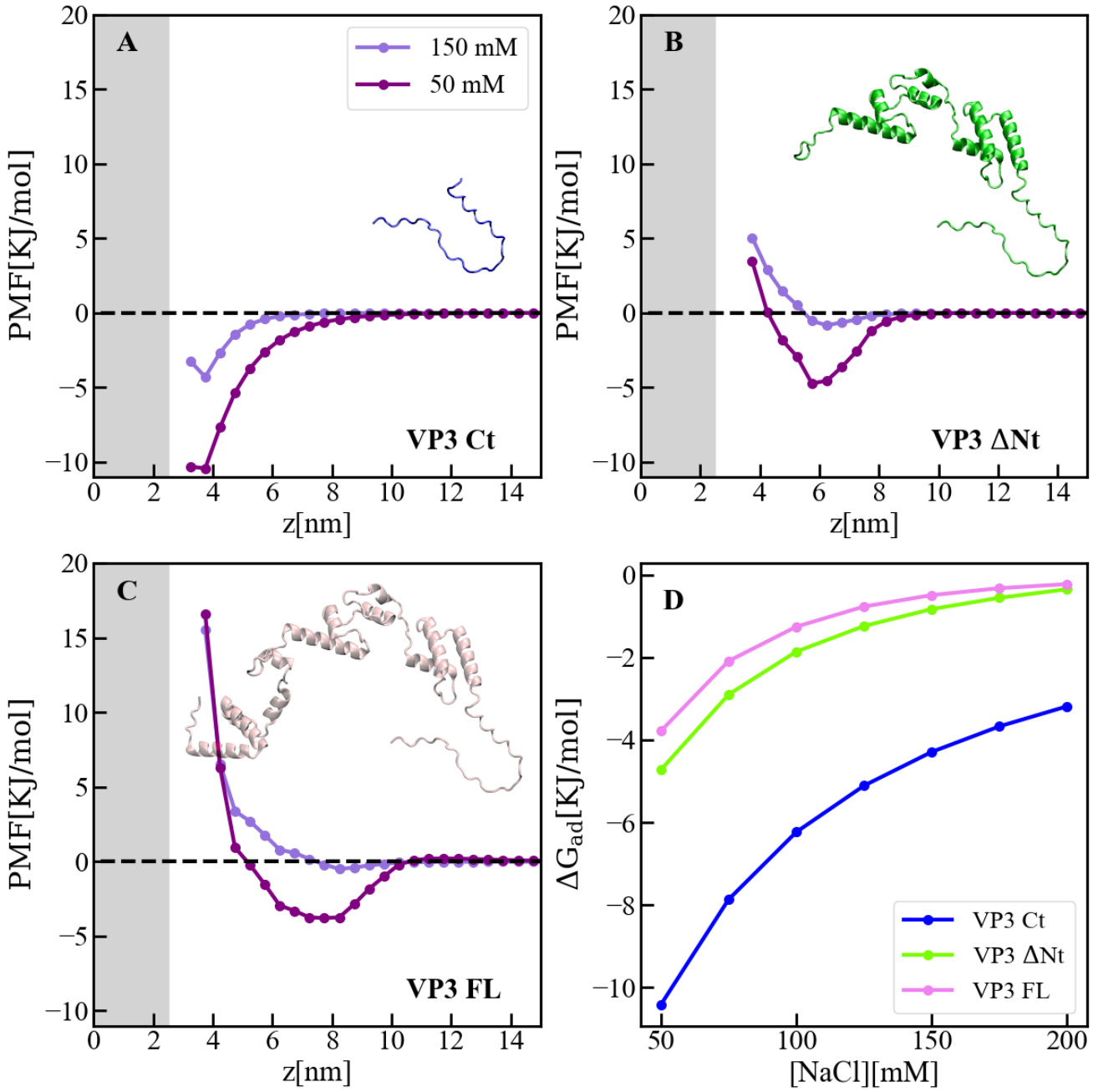

Figure 5. Adsorption of VP3 constructs to PI3P(+) model membranes.

(A-C). Adsorption free-energy profiles, PMF(z),for VP3 Ct, VP3 ΔNt and VP3 FL at 50 and 150 mM of NaCl.

(D) Adsorption free energy (ΔG_{ad}), computed from the minimum of PMF(z), versus concentration of NaCl. In all cases, the solution pH is 8, and the concentration of protein is 1 µM. The grey areas represent the volume excluded by half the membrane (cis hemilayer, z>0). The membrane surface contains 5% titratable groups, representing PI3P. Each group has three acidic moieties, one with a pKa of 2.5 and the others with 6.5. At 150 mM NaCl and pH 8, more than 90% of the acidic groups are deprotonated (*SI Appendix*, Fig. S5).

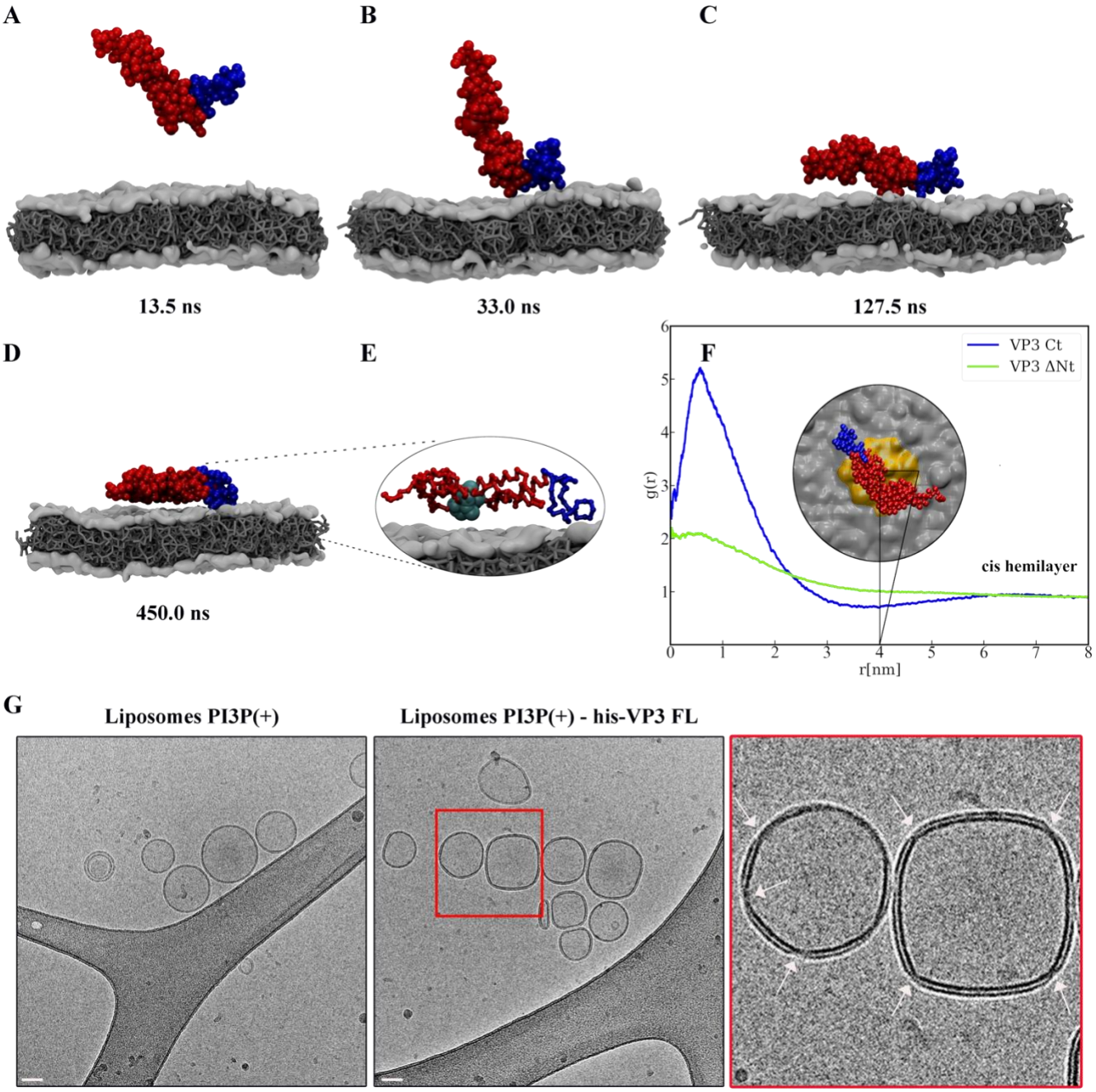

Figure 6. VP3 approaching a lipid bilayer, and distortion of the membrane.

(A-D) Temporal sequence of configurations illustrating how VP3 ΔNt approaches the negatively charged membrane during a 500 ns MD simulation. The membrane contains DOPE, DOPC and PI3P in 64:31:5 molar ratio. The beads making the Ct fragment are colored blue.

(E) Magnification of the protein configuration bound to the membrane, with P2 residues represented in cyan balls.

(F) Radial distribution function, g(r), between the center of mass of VP3 ΔNt and the center of PI3P molecules in the cis hemilayer. g(r) greater than 1 implies local enhancement of PI3P concentration. The inset shows an upper view of VP3 ΔNt bound to the membrane, with the area within r = 4 nm colored in orange.

(G) Cryo-electron microscopy images of cryo-fixated liposomes PI3P(+) control (without protein, left panel), or incubated with His-VP3 FL showing the small pinches or localized thinnings in the bilayer of the liposomes when His-VP3 FL was present (middle panel). The bar represents 50 nm. The right panel represents an enlarged image of the red square on the middle panel. White arrows point to the small pinches or localized thinnings in the bilayer when His-VP3 FL was present.

References

AnalystSoft Inc., StatPlus:mac - v8. n.d.

Baltimore D. 1971. Expression of animal virus genomes. *Bacteriol Rev* 35:235. doi:10.1128/BR.35.3.235-241.1971

Banani SF, Lee HO, Hyman AA, Rosen MK. 2017. Biomolecular condensates: organizers of cellular biochemistry. *Nat Rev Mol Cell Biol* 18:285–298. doi:10.1038/NRM.2017.7

Bolte S, Cordelières FP. 2006. A guided tour into subcellular colocalization analysis in light microscopy. *J Microsc* 224:213–232. doi:10.1111/j.1365-2818.2006.01706.x

Brodrick AJ, Broadbent AJ. 2023. The Formation and Function of Birnaviridae Virus Factories. *Int J Mol Sci* 24. doi:10.3390/IJMS24108471

Burd CG, Emr SD. 1998. Phosphatidylinositol(3)-phosphate signaling mediated by specific binding to RING FYVE domains. *Mol Cell* 2:157–62.

Casañas A, Navarro A, Ferrer-Orta C, González D, Rodríguez JF, Verdaguer N. 2008. Structural Insights into the Multifunctional Protein VP3 of Birnaviruses. *Structure* 16:29–37. doi:10.1016/j.str.2007.10.023

Chiarpotti M V., Longo GS, Del Pópolo MG. 2021. Nanoparticles modified with cell penetrating peptides: Assessing adsorption on membranes containing acidic lipids. *Colloids Surf B Biointerfaces* 197:111373. doi:10.1016/J.COLSURFB.2020.111373

Coulibaly F, Chevalier C, Gutsche I, Pous J, Navaza J, Bressanelli S, Delmas B, Rey FA. 2005. The birnavirus crystal structure reveals structural relationships among icosahedral viruses. *Cell* 120:761–772. doi:10.1016/j.cell.2005.01.009

Darden T, York D, Pedersen L. 1993. Particle mesh Ewald: An N·log(N) method for Ewald sums in large systems. *J Chem Phys* 98:10089–10092. doi:10.1063/1.464397

De Jong DH, Singh G, Bennett WFD, Arnarez C, Wassenaar TA, Schäfer L V., Periole X, Tieleman DP, Marrink SJ. 2013. Improved parameters for the martini coarse-grained protein force field. *J Chem Theory Comput* 9:687–697. doi:10.1021/ct300646g

Delgui LR, Rodriguez JF, Colombo MI. 2013. The Endosomal Pathway and the Golgi Complex Are Involved in the Infectious Bursal Disease Virus Life Cycle. *J Virol* 87:8993–9007. doi:10.1128/JVI.03152-12

Delmas B, Attoui H, Ghosh S, Malik YS, Mundt E, Vakharia VN. 2019. ICTV virus taxonomy profile: Birnaviridae. *Journal of General Virology* 100:5–6. doi:10.1099/jgv.0.001185

EMBL's European Bioinformatics Institute. n.d. https://www.ebi.ac.uk/

F Olson, C A Hunt FCS, W J Vail DP. 1979. Preparation of liposomes of defined size distribution by extrusion through polycarbonate membranes. *Biochim Biophys Acta* 557:9–23. doi:10.1016/0005-2736(79)90085-3

926 Fernandes F, Chen K, Ehrlich LS, Jin J, Chen MH, Medina GN, Symons M, Montelaro R, Donaldson J, Tjandra N,
927 Carter CA. 2011. Phosphoinositides Direct Equine Infectious Anemia Virus Gag Trafficking and Release.
928 *Traffic*. doi:10.1111/j.1600-0854.2010.01153.x

929 Gaullier J-M, Simonsen A, D'Arrigo A, Bremnes B, Stenmark H, Aasland R. 1998. FYVE fingers bind PtdIns(3)P.
930 *Nature 1998 394:6692* 394:432–433. doi:10.1038/28767

931 Ghanem A, Kern A, Conzelmann K-K. 2011. Significantly improved rescue of rabies virus from cDNA plasmids.
932 *Eur J Cell Biol* 91:10–16. doi:10.1016/j.ejcb.2011.01.008

933 Gibson DG, Young L, Chuang R-Y, Venter JC, Hutchison CA 3rd, Smith HO. 2009. Enzymatic assembly of DNA
934 molecules up to several hundred kilobases. *Nat Methods* 6:343–345. doi:10.1038/nmeth.1318

935 Gillooly DJ, Morrow IC, Lindsay M, Gould R, Bryant NJ, Gaullier JM, Parton RG, Stenmark H. 2000. Localization
936 of phosphatidylinositol 3-phosphate in yeast and mammalian cells. *EMBO Journal* 19:4577–4588.
937 doi:10.1093/emboj/19.17.4577

938 Gimenez MC, Issa M, Sheth J, Colombo MI, Terebiznik MR, Delgui LR. 2020. Phosphatidylinositol 3-Phosphate
939 Mediates the Establishment of Infectious Bursal Disease Virus Replication Complexes in Association with
940 Early Endosomes. *J Virol* 95:e02313-20. doi:10.1128/jvi.02313-20

941 Gimenez MC, Zanetti FA, Terebiznik MR, Colombo MI, Delgui LR. 2018. Infectious Bursal Disease Virus Hijacks
942 Endosomal Membranes as the Scaffolding Structure for Viral Replication. *J Virol* 92:e01964-17.
943 doi:10.1128/JVI.01964-17

944 Gorbalenya AE, Pringle FM, Zeddam JL, Luke BT, Cameron CE, Kalmakoff J, Hanzlik TN, Gordon KHJ, Ward VK.
945 2002. The palm subdomain-based active site is internally permuted in viral RNA-dependent RNA
946 polymerases of an ancient lineage. *J Mol Biol* 324:47–62. doi:10.1016/S0022-2836(02)01033-1

947 Gorvel JP, Chavrier P, Zerial M, Gruenberg J. 1991. rab5 controls early endosome fusion in vitro. *Cell* 64:915–25.

948 Johnson WC. 1999. Analyzing Protein Circular Dichroism Spectra for Accurate Secondary Structures. *Proteins*
949 35:307–312. doi:10.1002/(SICI)1097-0134(19990515)35:3

950 Jumper J, Evans R, Pritzel A, Green T, Figurnov M, Ronneberger O, Tunyasuvunakool K, Bates R, Žídek A,
951 Potapenko A, Bridgland A, Meyer C, Kohl SAA, Ballard AJ, Cowie A, Romera-Paredes B, Nikolov S, Jain R,
952 Adler J, Back T, Petersen S, Reiman D, Clancy E, Zielinski M, Steinegger M, Pacholska M, Berghammer T,
953 Bodenstein S, Silver D, Vinyals O, Senior AW, Kavukcuoglu K, Kohli P, Hassabis D. 2021. Highly accurate
954 protein structure prediction with AlphaFold. *Nature 2021 596:7873* 596:583–589. doi:10.1038/s41586-
955 021-03819-2

956 JustBio. n.d.

957 Kairys V, Baranauskiene L, Kazlauskiene M, Matulis D, Kazlauskas E. 2019. Binding affinity in drug design:
958 experimental and computational techniques. *https://doi.org/101080/1746044120191623202* 14:755–
959 768. doi:10.1080/17460441.2019.1623202

960 Kolli S, Meng X, Wu X, Shengjuler D, Cameron CE, Xiang Y, Deng J. 2015. Structure-Function Analysis of Vaccinia
961 Virus H7 Protein Reveals a Novel Phosphoinositide Binding Fold Essential for Poxvirus Replication. *J Virol*

962 89:2209–2219. doi:10.1128/JVI.03073-14/ASSET/F1575F5D-784E-4FD0-9DDB-
963 A2B374935CCA/ASSETS/GRAPHIC/ZJV9990900510007.JPEG

964 Komada M, Kitamura N. 1995. Growth factor-induced tyrosine phosphorylation of Hrs, a novel 115-kilodalton
965 protein with a structurally conserved putative zinc finger domain. *Mol Cell Biol* 15:6213–6221.
966 doi:10.1128/MCB.15.11.6213

967 Koonin E V., Dolja V V., Krupovic M, Varsani A, Wolf YI, Yutin N, Zerbini FM, Kuhn JH. 2020. Global Organization
968 and Proposed Megataxonomy of the Virus World. *Microbiology and Molecular Biology Reviews* 84.
969 doi:10.1128/MMBR.00061-19/SUPPL_FILE/MMBR.00061-19-S0001.PDF

970 Lees JG, Miles AJ, Wien F, Wallace BA. 2006. A reference database for circular dichroism spectroscopy covering
971 fold and secondary structure space. *Bioinformatics* 22:1955–1962. doi:10.1093/BIOINFORMATICS/BTL327

972 Lombardo E, Maraver A, Castón JR, Rivera J, Fernández-Arias A, Serrano A, Carrascosa JL, Rodriguez JF. 1999.
973 VP1, the putative RNA-dependent RNA polymerase of infectious bursal disease virus, forms complexes
974 with the capsid protein VP3, leading to efficient encapsidation into virus-like particles. *J Virol* 73:6973–83.

975 Luque D, Rivas G, Alfonso C, Carrascosa JL, Rodríguez JF, Castón JR. 2009a. Infectious bursal disease virus is an
976 icosahedral polyploid dsRNA virus. *Proc Natl Acad Sci U S A* 106:2148–52. doi:10.1073/pnas.0808498106

977 Luque D, Saugar I, Rejas MT, Carrascosa JL, Rodríguez JF, Castón JR. 2009b. Infectious Bursal Disease Virus:
978 Ribonucleoprotein Complexes of a Double-Stranded RNA Virus. *J Mol Biol* 386:891–901.
979 doi:10.1016/j.jmb.2008.11.029

980 Maraver A, Oña A, Abaitua F, González D, Clemente R, Ruiz-Díaz JA, Castón JR, Pazos F, Rodriguez JF. 2003. The
981 oligomerization domain of VP3, the scaffolding protein of infectious bursal disease virus, plays a critical
982 role in capsid assembly. *J Virol* 77:6438–49.

983 Marrink SJ, Risselada HJ, Yefimov S, Tieleman DP, De Vries AH. 2007. The MARTINI force field: Coarse grained
984 model for biomolecular simulations. *Journal of Physical Chemistry B* 111:7812–7824.
985 doi:10.1021/jp071097f

986 Matsuda T, Cepko CL. 2004a. Electroporation and RNA interference in the rodent retina in vivo and in vitro.
987 *Proc Natl Acad Sci U S A* 101:16–22. doi:10.1073/pnas.2235688100

988 Matsuda T, Cepko CL. 2004b. Electroporation and RNA interference in the rodent retina in vivo and in vitro.
989 *Proc Natl Acad Sci U S A* 101:16–22. doi:10.1073/PNAS.2235688100

990 Mcnulty S, Bornmann W, Schriewer J, Werner C, Smith SK, Olson VA, Damon IK, Buller RM, Heuser J, Kalman D.
991 2010. Multiple Phosphatidylinositol 3-Kinases Regulate Vaccinia Virus Morphogenesis. *PLoS One*
992 5:e10884. doi:10.1371/JOURNAL.PONE.0010884

993 Miles AJ, Wallace BA. 2018. CDtoolX, a downloadable software package for processing and analyses of circular
994 dichroism spectroscopic data. *Protein Science* 27:1717–1722. doi:10.1002/pro.3474

995 Nascimbeni AC, Codogno P, Morel E. 2017. Local detection of PtdIns3P at autophagosome biogenesis
996 membrane platforms. *Autophagy* 13:1602–1612. doi:10.1080/15548627.2017.1341465

997 Parrinello M, Rahman A. 1981. Polymorphic transitions in single crystals: A new molecular dynamics method. *J*
998 *Appl Phys* 52:7182–7190. doi:10.1063/1.328693

999 Periole X, Cavalli M, Marrink SJ, Ceruso MA. 2009. Combining an elastic network with a coarse-grained
1000 molecular force field: Structure, dynamics, and intermolecular recognition. *J Chem Theory Comput*
1001 5:2531–2543. doi:10.1021/CT9002114/SUPPL_FILE/CT9002114_SI_001.PDF

1002 Poma AB, Cieplak M, Theodorakis PE. 2017. Combining the MARTINI and Structure-Based Coarse-Grained
1003 Approaches for the Molecular Dynamics Studies of Conformational Transitions in Proteins. *J Chem Theory*
1004 *Comput* 13:1366–1374. doi:10.1021/ACS.JCTC.6B00986/ASSET/IMAGES/LARGE/CT-2016-
1005 00986K_0005.JPEG

1006 Potgieter AC, Page NA, Liebenberg J, Wright IM, Landt O, van Dijk AA. 2009. Improved strategies for sequence-
1007 independent amplification and sequencing of viral double-stranded RNA genomes. *J Gen Virol* 90:1423–
1008 1432. doi:10.1099/vir.0.009381-0

1009 Provencher SW, Glöckner J. 1981. Estimation of Globular Protein Secondary Structure from Circular Dichroism.
1010 *Biochemistry* 20:33–37. doi:10.1021/bi00504a006

1011 Puffer BA, Watkins SC, Montelaro RC. 1998. Equine infectious anemia virus Gag polyprotein late domain
1012 specifically recruits cellular AP-2 adapter protein complexes during virion assembly. *J Virol* 72:10218–
1013 10221. doi:10.1128/JVI.72.12.10218-10221.1998

1014 Qi X, Gao Y, Gao H, Deng X, Bu Z, Wang Xiaoyan, Fu C, Wang Xiaomei. 2007. An improved method for infectious
1015 bursal disease virus rescue using RNA polymerase II system. *J Virol Methods* 142:81–88.
1016 doi:10.1016/j.jviromet.2007.01.021

1017 Ramírez PG, Del Pópolo MG, Vila JA, Szleifer I, Longo GS. 2019. Adsorption and insertion of polyarginine
1018 peptides into membrane pores: The trade-off between electrostatics, acid-base chemistry and pore
1019 formation energy. *J Colloid Interface Sci* 552:701–711. doi:10.1016/J.JCIS.2019.05.087

1020 Reddy V, Lymar E, Hu M, Hainfeld JF. 2005. 5 nm Gold-Ni-NTA Binds His Tags. *Microscopy and Microanalysis*
1021 11:1118–1119. doi:10.1017/S1431927605507712

1022 Reddy VRAP, Campbell EA, Wells J, Simpson J, Nazki S, Hawes PC, Broadbent AJ. 2022. Birnaviridae Virus
1023 Factories Show Features of Liquid-Liquid Phase Separation and Are Distinct from Paracrystalline Arrays of
1024 Virions Observed by Electron Microscopy. *J Virol* 96:e0202421. doi:10.1128/jvi.02024-21

1025 RStudio Team. 2020. RStudio: Integrated Development Environment for R.

1026 Rydzanicz R, Zhao XS, Johnson PE. 2005. Assembly PCR oligo maker: a tool for designing oligodeoxynucleotides
1027 for constructing long DNA molecules for RNA production. *Nucleic Acids Res* 33:W521-5.
1028 doi:10.1093/nar/gki380

1029 Saugar I, Irigoyen N, Luque D, Carrascosa JL, Rodríguez JF, Castón JR. 2010. Electrostatic interactions between
1030 capsid and scaffolding proteins mediate the structural polymorphism of a double-stranded RNA virus. *J*
1031 *Biol Chem* 285:3643–50. doi:10.1074/jbc.M109.075994

1032 Schindelin J, Arganda-Carreras I, Frise E, Kaynig V, Longair M, Pietzsch T, Preibisch S, Rueden C, Saalfeld S,
1033 Schmid B, Tinevez J-Y, White DJ, Hartenstein V, Eliceiri K, Tomancak P, Cardona A. 2012. Fiji: an open-
1034 source platform for biological-image analysis. *Nat Methods* 9:676–682. doi:10.1038/nmeth.2019

1035 Shah NB, Duncan T, M. 2014. Bio-layer interferometry for measuring kinetics of protein-protein interactions
1036 and allosteric ligand effects. *J Vis Exp*. doi:10.3791/51383

1037 Sievers F, Wilm A, Dineen D, Gibson TJ, Karplus K, Li W, Lopez R, McWilliam H, Remmert M, Söding J, Thompson
1038 JD, Higgins DG. 2011. Fast, scalable generation of high-quality protein multiple sequence alignments using
1039 Clustal Omega. *Mol Syst Biol* 7:539. doi:10.1038/MSB.2011.75

1040 Simonsen A, Lippe R, Christoforidis S, Gaullier J-M, Brech A, Callaghan J, Toh B-H, Murphy C, Zerial M, Stenmark
1041 H. 1998. EEA1 links PI(3)K function to Rab5 regulation of endosome fusion. *Nature 1998 394:6692*
1042 394:494–498. doi:10.1038/28879

1043 Sreerama N, Woody RW. 2000. Estimation of protein secondary structure from circular dichroism spectra:
1044 Comparison of CONTIN, SELCON, and CDSSTR methods with an expanded reference set. *Anal Biochem*
1045 287:252–260. doi:10.1006/abio.2000.4880

1046 Stenmark H, Aasland R, Toh BH, D'Arrigo A. 1996. Endosomal localization of the autoantigen EEA1 is mediated
1047 by a zinc-binding FYVE finger. *J Biol Chem* 271:24048–54.

1048 Tanzi GO, Piefer AJ, Bates P. 2003. Equine infectious anemia virus utilizes host vesicular protein sorting
1049 machinery during particle release. *J Virol* 77:8440–8447. doi:10.1128/JVI.77.15.8440-8447.2003

1050 Valli A, Busnadiego I, Maliogka V, Ferrero D, Castón JR, Rodríguez JF, García JA. 2012. The VP3 Factor from
1051 Viruses of Birnaviridae Family Suppresses RNA Silencing by Binding Both Long and Small RNA Duplexes.
1052 *PLoS One* 7:e45957. doi:10.1371/journal.pone.0045957

1053 Walker PJ, Siddell SG, Lefkowitz EJ, Mushegian AR, Adriaenssens EM, Alfenas-Zerbini P, Davison AJ, Dempsey
1054 DM, Dutilh BE, García ML, Harrach B, Harrison RL, Hendrickson RC, Junglen S, Knowles NJ, Krupovic M,
1055 Kuhn JH, Lambert AJ, Łobocka M, Nibert ML, Oksanen HM, Orton RJ, Robertson DL, Rubino L,
1056 Sabanadzovic S, Simmonds P, Smith DB, Suzuki N, Van Dooerslaer K, Vandamme AM, Varsani A, Zerbini
1057 FM. 2021. Changes to virus taxonomy and to the International Code of Virus Classification and
1058 Nomenclature ratified by the International Committee on Taxonomy of Viruses (2021). *Arch Virol*
1059 166:2633–2648. doi:10.1007/S00705-021-05156-1

1060 Wassenaar TA, Ingólfsson HI, Böckmann RA, Tieleman DP, Marrink SJ. 2015. Computational lipidomics with
1061 insane: A versatile tool for generating custom membranes for molecular simulations. *J Chem Theory*
1062 *Comput* 11:2144–2155. doi:10.1021/acs.jctc.5b00209

1063 Whitmore L, Wallace BA. 2008. Protein secondary structure analyses from circular dichroism spectroscopy:
1064 Methods and reference databases. *Biopolymers* 89:392–400. doi:10.1002/bip.20853

1065 Whitmore L, Wallace BA. 2004. DICHROWEB, an online server for protein secondary structure analyses from
1066 circular dichroism spectroscopic data. *Nucleic Acids Res* 32. doi:10.1093/nar/gkh371

1067 Wickham H. 2016. ggplot2: Elegant Graphics for Data Analysis. Springer-Verlag New York.

1068 Wills JW, Craven RC. 1991. Form, function, and use of retroviral gag proteins. *AIDS* 5:639–654.
1069 doi:10.1097/00002030-199106000-00002

1070 Yanai H, Hayashi Y, Watanabe Y, Ohtaki N, Kobayashi T, Nozaki Y, Ikuta K, Tomonaga K. 2006. Development of a
1071 novel Borna disease virus reverse genetics system using RNA polymerase II promoter and SV40 nuclear
1072 import signal. *Microbes Infect* 8:1522–1529. doi:10.1016/j.micinf.2006.01.010

1073 Zhou L, Feng T, Xu S, Gao F, Lam TT, Wang Q, Wu T, Huang H, Zhan L, Li L, Guan Y, Dai Z, Yu G. 2022. ggmsa: a
1074 visual exploration tool for multiple sequence alignment and associated data. *Brief Bioinform* 23.
1075 doi:10.1093/BIB/BBAC222

1076